Effect of Aerosols on Freezing Drops, Hail, and Precipitation in a Midlatitude Storm

EYAL ILOTOVIZ AND ALEXANDER P. KHAIN

Department of Atmospheric Sciences, Hebrew University of Jerusalem, Jerusalem, Israel

NIR BENMOSHE

NOAA/Geophysical Fluid Dynamics Laboratory, Princeton, New Jersey

VAUGHAN T. J. PHILLIPS

Department of Physical Geography and Ecosystem Science, Lund University, Lund, Sweden

ALEXANDER V. RYZHKOV

Cooperative Institute for Mesoscale Meteorological Studies, University of Oklahoma, Norman, Oklahoma

(Manuscript received 20 May 2014, in final form 18 April 2015)

ABSTRACT

A midlatitude hail storm was simulated using a new version of the spectral bin microphysics Hebrew University Cloud Model (HUCM) with a detailed description of time-dependent melting and freezing. In addition to size distributions of drops, plate-, columnar-, and branch-type ice crystals, snow, graupel, and hail, new distributions for freezing drops as well as for liquid water mass within precipitating ice particles were implemented to describe time-dependent freezing and wet growth of hail, graupel, and freezing drops.

Simulations carried out using different aerosol loadings show that an increase in aerosol loading leads to a decrease in the total mass of hail but also to a substantial increase in the maximum size of hailstones. Cumulative rain strongly increases with an increase in aerosol concentration from 100 to about 1000 cm^{-3}. At higher cloud condensation nuclei (CCN) concentrations, the sensitivity of hailstones' size and surface precipitation to aerosols decreases. The physical mechanism of these effects was analyzed. It was shown that the change in aerosol concentration leads to a change in the major mechanisms of hail formation and growth. The main effect of the increase in the aerosol concentration is the increase in the supercooled cloud water content. Accordingly, at high aerosol concentration, the hail grows largely by accretion of cloud droplets in the course of recycling in the cloud updraft zone. The main mechanism of hail formation in the case of low aerosol concentration is freezing of raindrops.

1. Introduction

Simulation of hail formation in midlatitude storms is one of the important problems in cloud physics. Hailstorms pose a serious threat to agriculture and property in many places around the world. During the last few decades, much effort has been devoted to understanding the physical and dynamic processes favoring hail formation [see Cotton and Anthes (1989) for a comprehensive review]. Most studies point out that convective instability, high atmospheric humidity, and moderate wind shear favor the development of intense hailstorms. Foote (1984) stresses that hailstone size is strongly affected by the width and tilt of the main updraft. According to Browning and Foote's (1976) hailstone growth model, small frozen hydrometeors, or hailstone embryos, fall from the back-sheared anvil (referred to as the "embryo curtain") and become reingested in the updraft, where they accrete liquid water during their final ascent through the updraft. The largest hailstones grow in a favored region of moderate updraft strength, where the hailstone fall velocity approximately balances the updraft speed. Using a spectral bin microphysics model, Takahashi

Corresponding author address: Prof. Alexander Khain, Department of Atmospheric Sciences, Institute of Earth Sciences, Hebrew University of Jerusalem, Givat Ram, Jerusalem 91904, Israel.
E-mail: alexander.khain@mail.huji.ac.il

DOI: 10.1175/JAS-D-14-0155.1

(1976) also found that the recycling of hail within cloud updrafts was a key factor in its growth. In the Takahashi model, recycled ice crystals lead first to graupel formation. At the last stage of the storm process hail falls in the cloud center, growing by accretion of cloud droplets.

The importance of hail embryo recycling for hail growth was noted by Nelson (1983) as well. This researcher analyzed multiple-Doppler data and used a simple particle growth model in which a hail embryo grows within a given field of vertical velocity and cloud water content. Tessendorf et al. (2005) analyzed the kinematics and microphysics of the 29 June supercell storm observed during the Severe Thunderstorm Electrification and Precipitation Study (STEPS) field campaign using polarimetric and Doppler radar data. They found that most of the largest hail grew from near-millimeter-sized particles that originated in the mid- to upper-level stagnation region that resulted from an obstacle-like flow of environmental air around the divergent outflow from the upper part of the updraft. These recycling embryonic particles descended around the right flank of the updraft core and reentered the updraft, intermingling with other smaller particles that had grown from cloud base along the main low-level updraft stream.

Using the Regional Atmospheric Modeling System (RAMS) with a bin-emulating two-moment bulk scheme, Seigel and van den Heever (2013) simulated an idealized squall line. They showed that the entrainment of hail and rain into the upwind side of the updraft below the freezing level leads not only to growth of hail but to extra latent heat release that, in turn, enhances buoyancy and precipitation. These observational and numerical results indicate that hail grows largely by accretion of supercooled water in the course of hail embryo recycling.

Thus, the mass of supercooled water would be expected to substantially affect the size of hail particles. Hail suppression hypotheses suggest that in order to prevent hail embryos from growing to hailstone size, the amount of supercooled water should be decreased (T. W. Krauss 1999, conference lecture; Wisner et al. 1972; Heymsfield 1982). Since an increase in the concentration of cloud condensation nuclei (CCN) typically leads to an increase in supercooled water content (Ramanathan et al. 2001; Andreae et al. 2004; Rosenfeld et al. 2008; Freud et al. 2008; Khain 2009), it would be expected that CCN would have a strong effect on the mass and the size of hail particles.

To describe aerosol effects on hail mass content (HMC) and hail size, models with advanced microphysics are required (Levin and Cotton 2009; Khain 2009; Tao et al. 2007, 2012). In numerous bulk-parameterization schemes, number size distributions of precipitating particles, including those for hail, are assumed in the form of gamma or exponential distributions. Since the size of large hail corresponds to the right tail of the distributions, the tail of the distribution should be properly described. For instance, Farley and Orville (1986) included in their bulk-parameterization scheme elements of bin microphysical schemes in which hail is calculated using a mass grid containing several tens of bins. To simulate hail with diameters exceeding 1 cm, Noppel et al. (2010) included a new hydrometeor class of hail into Seifert and Beheng's (2006) two-moment bulk-parameterization scheme. In some three-moment bulk-parameterization schemes (e.g., Milbrandt and Yau 2005; Dawson et al. 2014; Loftus and Cotton 2014a,b; Loftus et al. 2014) the shape parameter of the gamma distribution is also predicted, thus permitting more flexibility in the simulated hail distribution functions. Loftus and Cotton (2014a) and Loftus et al. (2014) showed that a three-moment bulk parameterization can describe the formation of observed hail size much more realistically than a two-moment bulk-parameterization scheme.

Despite the significant progress in the development of advanced microphysical schemes, aerosol effects on HMC and hail size have been investigated in only a handful of studies (Khain et al. 2011; Loftus and Cotton 2004b). Of particular interest is the influence of CCN on the formation and size of hail. According to the conceptual hypothesis formulated in the European project Anthropogenic Aerosols Triggering and Invigorating Severe Storms (ANTISTORM), by fostering an increase in supercooled water mass aloft, aerosols promote an increase in hail mass and size (Rosenfeld and Khain 2008). To test the ''ANTISTORM'' hypothesis, a hail storm that was observed in southwest Germany on 28 June 2006 was simulated using two models: the Hebrew University Cloud Model (HUCM) using spectral bin microphysics (SBM) (Khain et al. 2011) and the weather-prediction model Consortium for Small-Scale Modelling (COSMO) using Seifert and Beheng's (2006) two-moment bulk microphysical scheme with a special hydrometeor class of large hail (Noppel et al. 2010). While the main characteristics of the hail storm were reproduced by both models, the aerosol effects turned out to be different. HUCM predicted a substantial increase in hail size, radar reflectivity, and accumulated rain mass with increasing CCN concentration (Khain et al. 2011), while the two-moment bulk-parameterization COSMO predicted a decrease in hail size and precipitation with increasing CCN concentration (Noppel et al. 2010).

This discrepancy reflects the complexity of the mechanisms of hail formation and growth and the need to treat the process of hail formation and growth with the most detailed microphysical schemes available.

Notably, numerical models typically assume that freezing of supercooled drops immediately leads to hail formation. At the same time, the process of raindrop freezing is time dependent and the time needed for complete freezing of a raindrop may reach a few minutes (Pruppacher and Klett 1997; Phillips et al. 2014, 2015). During this time, the freezing drops (FDs) can be transported by convective and background flows over distances of several hundred meters to a few kilometers. Continuous accretion of supercooled droplets by freezing drops increases the freezing time. Properties of freezing drops such as liquid water fraction, particle shape, bulk density, and fall velocity change with time in the course of the freezing process. In this sense, freezing drops differ both from raindrops and hail and actually represent a separate type of hydrometeor.

Large raindrops are nonspherical and have a preferred orientation. Accordingly, they produce large values of differential reflectivity Z_{DR} measured by dual-polarimetric Doppler radars. Since FDs contain both liquid and water fractions, FDs tumble. Accordingly, the values of Z_{DR} caused by FDs are smaller than that of raindrops. However, FDs still play an important role in the mechanism of the formation of so-called Z_{DR} columns—that is, zones of enhanced Z_{DR} [Kumjian et al. (2014) and references therein]. The spatial distribution of FDs affects the rate of hail formation and the spatial location of the zones in which hail forms.

The regime of FDs' and hail growth, dry or wet, is important not only for an understanding of the layered structure of hail particles but also for the correct calculation of their growth rate. Hail in the dry growth regime—that is, when its surface is dry—cannot collect ice particles. In contrast, hail particles growing in the regime of wet growth are covered by a liquid water film and can collect ice particles. Fall velocities of FDs, graupel, and hail also depend on the growth regime, since dry and wet surfaces have different surface roughness. Equally, the wet growth process determines the vertical distribution of latent heat release from freezing, which influences the cloud dynamics. The theory of wet growth (Pruppacher and Klett 1997; List 2014a,b) was recently extended to the case in which liquid skin covers only a fraction of graupel or hail particles (Phillips et al. 2014, 2015). The theory of wet growth of hail developed by Phillips et al. (2014) allowed a numerical reproduction of the results of Garcia-Garcia and List's (1992) laboratory experiments.

Cloud microphysical models tend to assume that all water at the surface of hail particles growing in the regime of wet growth immediately sheds. This assumption simplifies the scheme of hail growth but is physically incorrect. To properly simulate the process of wet growth of graupel and hail, it is necessary to take into account the existence of liquid water within these particles. Phillips et al. (2014) consider a multilayered structure of hail stones containing the core, the sponge layer, and the liquid layer at the surface. The type of hail or graupel growth is determined in the scheme by the temperature of the particle surface. Since the freezing of liquid in the sponge layer takes some time (depending on environmental conditions), hail that started growing by dry growth may contain interior liquid accumulated for the periods of previous wet growth.

The theoretical scheme by Phillips et al. (2014, 2015) has been implemented into HUCM. The aim of this study is to investigate the role of aerosols in the formation and growth of FDs and hail in a mixed-phase convective storm. We examine the effects of aerosols on the size distribution, mass, and growth regime of FDs and hail and, subsequently, on cloud microphysical structure and precipitation patterns.

2. Model description

The HUCM is a two-dimensional nonhydrostatic model using spectral bin microphysics. The main components of the model are described in Khain and Sednev (1996) and Khain et al. (2004, 2008, 2012). In the new version of the model, the size distributions for eight hydrometeors are predicted (drops, three types of ice crystals, snow, graupel, hail, and freezing drops). The types of ice crystals are plates, columns, and branch type (dendrites). The size distributions are defined on the logarithmic equidistant mass grid containing 43 mass-doubling bins for each microphysical species. The mass corresponding to the smallest bin is equal to that of a liquid droplet with a radius of 2 μm. The cloud–aerosol interaction is described by means of a size distribution of aerosol particles (AP) playing the role of CCN. The AP size distribution also contains 43 bins. The radius of dry AP ranges from 0.005 to 2 μm. The main particle characteristic is particle mass. The properties of ice crystals and aggregates like density, aspect ratios, and fall velocity are determined using the empirical power law relationships presented by Pruppacher and Klett (1997) (see also Khain and Sednev 1995; Khain et al. 2004; Mitchell 1996). Diffusional growth of all particles is calculated by solving analytically the equation system for particle size and supersaturations with respect to water and ice, so that the supersaturation values change during the model time step in the course of the diffusional growth.

Collisions between different particles are calculated by solving a system of stochastic kinetic equations for collisions using the computationally efficient and accurate

method proposed by Bott (1998). Height-dependent, gravitational collision kernels for drop–drop and drop–graupel interactions are adapted from Pinsky et al. (2001) and Khain et al. (2001) and for collisions between ice crystals from Khain and Sednev (1995) and Khain et al. (2004). It was assumed that if FDs grow in the wet growth regime (i.e., they are covered by liquid film), FDs can collect graupel and ice crystals. Effects of turbulence on collisions between cloud drops are included, following Benmoshe et al. (2012).

The ice nuclei concentration depends on supersaturation with respect to ice, as described by the empirical expression of Meyers et al. (1992). Primary nucleation of each ice crystal type occurs within its characteristic temperature range (Takahashi et al. 1991). Secondary ice generation is accounted for during riming (Hallett and Mossop 1974).

The initial ($t = 0$) CCN size distribution is calculated using the empirical dependence $N_{\rm CCN} = N_o S_w^k$, where S_w is supersaturation with respect to water and N_o and k are the measured constants (Khain et al. 2000). The prognostic equation for the size distribution of nonactivated AP is solved for $t > 0$. Using the value of S_w calculated at each time step, the critical radius of CCN is determined according to the Köhler theory. The CCN with radii exceeding the critical value are activated, and new droplets are nucleated. The corresponding bins of the CCN size distributions become empty. In the present study, CCN consist of NaCl. As shown by Khain et al. (2000), the chemical composition of CCN is not of crucial importance as regards the process of CCN nucleation. The most important parameter of CCN is their size. The utilization of large number of bins allows for a precise description of droplet concentration.

Time-dependent melting of snow, graupel, and hail as well as shedding of water from hail was implemented into the HUCM following the work of Phillips et al. (2007). The new components of the scheme are implementation of FDs as a new hydrometeor type and using the procedure of time-dependent freezing. Precipitating ice particles such as graupel, hail, and FDs can contain unfrozen liquid at freezing temperatures. Freezing of the liquid is described by solving the corresponding heat balance equations at the particle surface and at the ice–liquid interfaces, according to Phillips et al. (2014, 2015). The balanced equations are written in the most general form that takes into account the thermodynamic effects of accretion of drops and ice crystals, as well as of shedding. At $T < 0$°C, the water mass within FDs, graupel, and hail is advected, mixed, and sedimented exactly as the size distribution of corresponding particles. For snow, water fraction is only tracked for $T > 0$°C, whereas for FDs, it is only tracked for $T < 0$°C. For graupel and hail, water fraction is tracked at all temperatures.

The implementation of the mass of water within ice particles allows for the calculation of successive processes of melting and freezing during particle oscillation around the freezing level of environmental temperature.

The implementation of FDs as a new class of hydrometeor has involved changing the scheme for the conversion of hydrometeors (Fig. 1). FDs form as a result of two processes: the heterogeneous ice nucleation in raindrops (''nucleation drop freezing'') and the collision of drops with ice particles of less mass than the drops. In HUCM, FDs form by ''nucleation'' (or immersion) freezing of raindrops with radii exceeding 100 $\rm cm^{-3}$. Freezing of smaller droplets is assumed to lead to the formation of ice crystal (plates) with a density of 0.92 $\rm g\,cm^{-3}$.

According to Pruppacher and Klett (1997), the process of nucleation drop freezing consists of two stages. During the first, very short stage (nucleation–immersion or contact), an ice germ forms either on nonsoluble ice nuclei (IN) or spontaneously. Within the temperature range $-30° \le T \le -40$°C the fraction of droplets involved in the first stage of freezing is determined by the formula of probabilistic freezing formulation (Bigg 1953; Wisner et al. 1972; Reisner et al. 1998; Khain and Sednev 1996). At warmer temperatures, the fraction of droplets involved in the first stage of freezing is determined following Vali (1994), who described the temperature dependence of immersion nuclei [see Khain et al. (2004) for details]. Droplets that have passed through the nucleation drop freezing stage are converted into FDs. The mass of ice m_i in newly formed FDs is determined by the heat balance of an isolated particle of mass m (Pruppacher and Klett 1997; Phillips et al. 2015):

$$m_i L_m = [f_L m c_w + (1 - f_L) m c_i] \Delta T, \qquad (1)$$

where f_L is the liquid fraction of the FD. The initial f_L before the first freezing stage is equal to one. ΔT is the increase in temperature of the drop during the first stage ($\Delta T = 273.5 - T$), where $T < 0$°C is the environmental temperature and c_w and c_i are specific heat capacities for water and ice, respectively. The quantity L_m is the latent heat of freezing.

The second stage of freezing is a comparatively long thermodynamic process of ice growth within a drop until its total freezing. The initial value of ice mass in FDs is determined by Eq. (1). The freezing takes place from the outside in. In the absence of the accretion of supercooled droplets, the surface of FDs remains dry and the interior liquid freezes because of an outward-directed

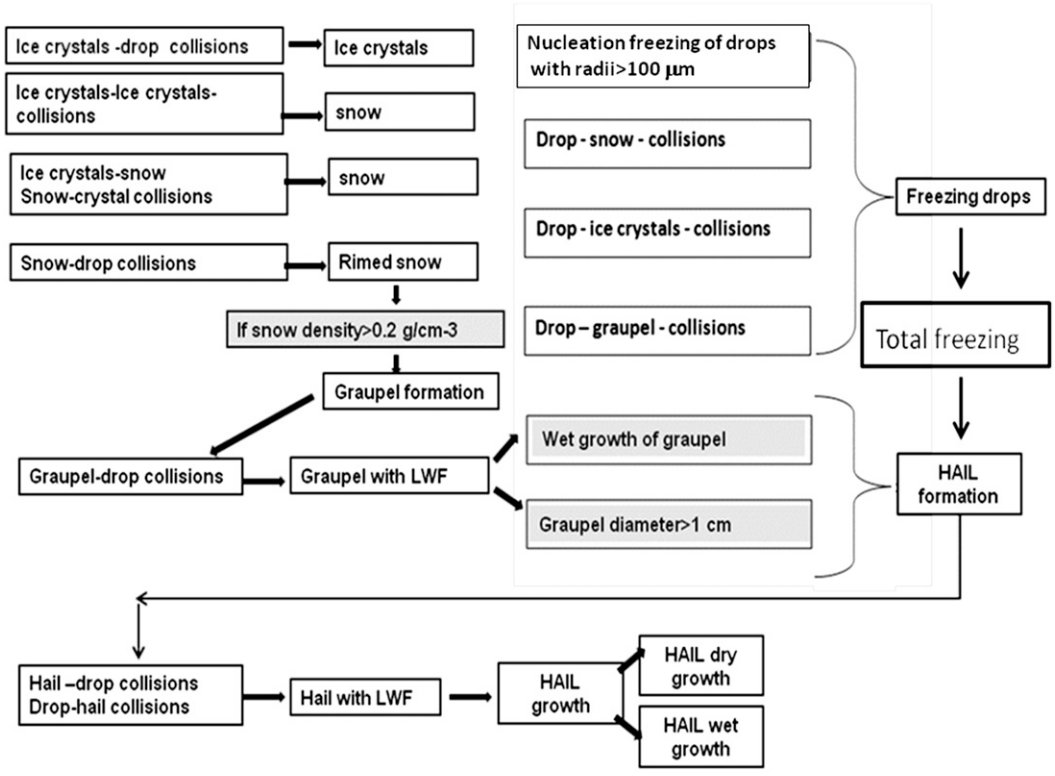

FIG. 1. Schematic illustration of mechanisms leading to formation of graupel, freezing drops, and hail in the HUCM. The hydrometeor listed first in the collision process is larger than the second one. LWF is liquid water fraction.

heat flux. During this process, the ice shell depth increases. The process of freezing in this case is described following Pruppacher and Klett (1997, p. 678). If FDs collect supercooled droplets, both dry and wet growths of FDs are possible. To determine the type of growth, the surface particle temperature T_s is calculated using the heat balance equation at the particle surface. Dry growth occurs when the surface temperature is $T_s < 273.15$. Otherwise, the FD is assumed to grow in a wet growth regime. In this case, the freezing of interior liquid is terminated [see Phillips et al. (2015) for details]. FDs transfer into hail if the liquid water fraction (LWF) is less than 0.1. The interior liquid remains in the particle during the transformation.

The fall velocity of FDs and hail particles is calculated following Rasmussen and Heymsfield (1987, appendix B therein) and Phillips et al. (2015). The approach is based on the calculation of the drag coefficient C_d using the C_d–Re relationship, where Re is the Reynolds number. In turn, Re is determined from the Re–X relationship, where $X = \mathrm{Re}^2 C_d(\mathrm{Re})$ is the Best number. The Best number depends on particle mass and environment air parameters. This approach takes into account the change of fall velocity when dry growth is replaced by wet growth, and vice versa. The liquid water fraction (f_L) of an FD decreases during freezing. As f_L in an FD becomes less than 10%, the FD is converted to a hailstone of corresponding mass (Fig. 1). A detailed description of the melting of FDs would require us to treat the evolution of three layers: the interior liquid, ice layer, and exterior liquid. Such calculations are too complicated and uncertain. So, as soon as FDs fall below the melting level they are converted into melting hail. Note that FDs typically freeze and convert to hail. So, the downward flux of FDs through the melting level is typically very low.

There is a fundamental difference between the behavior of FDs and raindrops. While large raindrops become unstable and breakup occurs, FDs are covered by an ice shell and are thus stable. So, FDs do not experience breakup and reach larger sizes than raindrops.

In the new HUCM version, hail forms in three ways: total freezing of FDs, conversion of graupel growing in the regime of wet growth, and conversion of graupel particles exceeding 1 cm in diameter (Fig. 1). The density of hail is assumed equal to 0.92 g cm^{-3}. The rate of freezing of accreted water at the surface of graupel and hail particles is also calculated by solving corresponding heat budget equations. During these collisions, freezing

is also separated into two stages: the nucleation stage and the longer time-dependent freezing stage. After a collision occurs, a fraction of the water determined by Eq. (1) freezes immediately. The rest of the liquid water freezes comparatively slowly.

The processes of wet and dry growth of graupel and hail are considered during the time-dependent freezing, as described by Phillips et al. (2014). One of the specific features of wet growth is the shedding of water film and the consequent production of new raindrops. Different microphysical schemes take into account effects of shedding at different levels of complexity. Many bulk schemes, for example Lin et al. (1983), compute shedding without explicit treatment of time-dependent freezing. It is typically assumed that all melted water is immediately shed. In the context of immediate freezing, as in Khain et al. (2011), shedding of hail in the HUCM takes place only during melting. In this study, a detailed description of shedding in wet growth is included in the microphysical scheme. In this scheme of time-dependent freezing, shedding of liquid drops from the surface of hail takes place during wet growth at $T < 0°C$ as well. The shedding takes place if both the mass of exterior liquid water and the mass of hail particles exceed their critical values. The size of raindrops forming as a result of shedding depends on Re (Rasmussen and Heymsfield 1987). According to Rasmussen and Heymsfield (1987), melting ice spheres shed part of their meltwater (in the form of water drops) if the mass of water on the surface of the ice core exceeds the critical value M_{w_crit} that is linearly dependent on the ice mass M_i in the melting particle:

$$M_{w\_crit} = 0.268 + 0.1389 M_i. \quad (2)$$

The condition (2) determines the minimum size of hail that melts to a raindrop without shedding. This condition also determines the maximum liquid water fraction at which hail is able to shed liquid water. Following Phillips et al. (2007), we assumed that the shed water mass cannot exceed 50% of the critical water mass.

In the present study, we neglect shedding from the surface of FDs. FDs typically contain interior liquid water that is surrounded by an ice shell. So, there is no shedding from FDs. In agreement with laboratory results, no shedding from snow takes place (Phillips et al. 2007). Since graupel that starts growing by wet growth is converted to hail, there is no shedding from graupel.

The implementation of FDs substantially changes the process of hail formation, as compared to that considered by Khain et al. (2011). While in the version by Khain et al. (2011) liquid droplet–ice collisions (e.g., liquid drop–snow collisions) led to the formation of graupel, in cases of time-dependent freezing these collisions led to FD formation (Fig. 1). The properties of FDs (fall velocities, sticking efficiencies) are closer to those of hail than of graupel (whose density was taken equal to $0.4\,g\,cm^{-3}$). As a result, FDs grow faster by accretion of cloud droplets than graupel, which leads, as will be shown below, to an increase of hail size as compared to that simulated by Khain et al. (2011).

Accretion of liquid droplets accreted by aggregates (snow) leads to soaking and total freezing with the formation of rimed mass with the density of pure ice $0.92\,g\,cm^{-3}$. The bulk density of snow increases in the course of riming. To calculate bulk density, the mass of rimed (frozen) water within snow is calculated. This mass is advected, mixed, and sedimented exactly as the size distribution of snow. Rimed snow with a bulk density exceeding $0.2\,g\,cm^{-3}$ is typically attributed to a class of graupel, whose density in clouds varies from 0.2 to $0.8\,g\,cm^{-3}$ (Pruppacher and Klett 1997). So, if the bulk density of snow exceeds $0.2\,g\,cm^{-3}$, the rimed snow is converted to graupel (Fig. 1). At present, graupel in the model is characterized by the typical graupel density of $0.4\,g\,cm^{-3}$.

Graupel is converted to hail in two cases: graupel starts growing by wet growth or if graupel reaches 1 cm in diameter. Note that time-dependent freezing takes into account the process of suction of liquid into the interior of particles. The liquid can remain at the surface of particle only in case when the air in the particle is replaced by water. So, as soon as graupel starts growing by wet growth, its density should be considered as large as of that of hail.

The implementation of variable density of graupel will be performed in future studies as it is used for aggregates, applying the approaches developed by Milbrandt and Morrison (2013).

The turbulence in the model is described using the 1.5 closure scheme, according to which turbulent coefficients are calculated using the equation for turbulent kinetic energy. Following Benmoshe et al. (2012), the effects of turbulence on collisions between cloud droplets are taken into account.

3. Design of simulations

All simulations were performed within a computational domain of 153.9 km × 19.2 km and a grid spacing of 300 m in the horizontal direction and 100 m in the vertical direction. The new microphysical scheme was tested in simulations of a thunderstorm observed in Villingen-Schwenningen, southwest Germany, on 28 June 2006. The meteorological conditions of this storm were described by (Khain et al. 2011). In particular, the sounding was presented in Fig. 1 of that study. The background wind

direction was quasi 2D, which simplified the prescription of the background wind profile in the 2D model. The wind speed increased with height from ~10 m s^{-1} in the lower atmosphere to about 20 m s^{-1} at levels of 100–200 hPa. In Villingen-Schwenningen, the daily maximum air temperature near the surface reached 22.9°C at 1500 UTC. The value of CAPE calculated using available sounding was comparatively low (from 759 to ~1240 J kg^{-1}), but given the temporal and spatial delay and the observed temperature maximum at Villingen-Schwenningen, the CAPE greater than 1800 J kg^{-1} probably reflected the development of a convective boundary layer in the afternoon after the radiosonde measurements. Such a value was used in simulations of this storm by Noppel et al. (2010) and Khain et al. (2011). The relative humidity near the ground was high (~85%), which led to a low lifting condensation level of about 890 m. The freezing level was located around 3.5 km. The observed maximum diameter of hailstones was about 5 cm.

The convection was initiated by a 20-min temperature decrease (cooling) near the left boundary of the computational area within the area situated from 18 to 43 km in the horizontal direction and 2-km depth. The rate of cooling was 0.0084 K s^{-1}. This type of storm initiation is traditionally used to initiate squall lines (Rotunno and Klemp 1985).

G. Frank and U. Dusek (Department of Biogeochemistry, Max Planck Institute for Chemistry, 2008, personal communication) approximated the dependence of CCN concentration on supersaturation, measured near the surface just before the storm, by the dependence $N_{CCN} = N_o S_w^k$ with $N_o = 3300\,\text{cm}^{-3}$ and slope parameter $k = 0.5$. Such a high value of N_o indicates that the storm developed in highly polluted air. The same conclusion was reached in simulations by S. Metzger (2007, personal communication) using the ECHAM5/Modular Earth Submodel System (MESSy) model.

To investigate effects of CCN concentration on hail formation, six simulations were performed for different CCN concentrations (at 1% of supersaturation) ranging from 100 to 5000 cm^{-3}. All simulations can be separated into two groups of low CCN concentration (100 and 400 cm^{-3}) and high CCN concentrations. These simulations are referred to as L_CCN and H_CCN, respectively. Below, we will often use the names L_CCN and H_CCN for the two particular runs with CCN concentrations of 100 and 3000 cm^{-3}, respectively.

4. Results of simulations

a. *Major aerosol effects on cloud microphysics and dynamics*

In many studies, the aerosol-induced convective invigoration is reported (e.g., Khain et al. 2004, 2008; Rosenfeld et al. 2008; Khain 2009). This invigoration is characterized by an increase in the maximum updraft velocity, cloud turbulence, and, sometimes, the cloud-top height. Such invigoration is typical of tropical maritime convection, where warm rain contributes significantly to heat and precipitation budgets. An increase in the CCN concentration under tropical conditions increases the residential time of droplets within clouds and leads to an intensification of ice processes accompanied by a latent heat release and an increase in the vertical velocity.

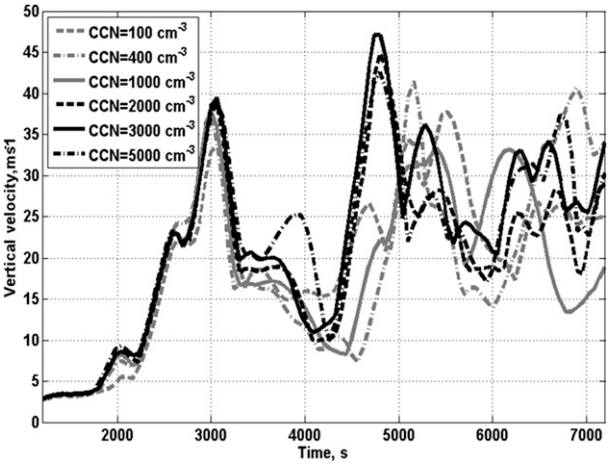

FIG. 2. Time dependencies of maximum vertical velocities in simulations with different CCN concentrations shown by the different lines from 100 to 5000 cm^{-3}.

To give an idea of CCN effects on the dynamics of a midlatitude storm, we present Fig. 2 showing time dependencies of maximum vertical velocities in simulations with different CCN concentrations. Despite the fact that the maximum vertical velocities in the case of high CCN concentration (CCN concentration above 1000 cm^{-3}) are a few meters per second larger than in the case of the low CCN concentration (CCN concentration 100–400 cm^{-3}), Fig. 2 does not reveal a strong sensitivity of vertical velocity maxima to CCN concentration, at least for CCN concentrations exceeding 500–1000 cm^{-3}. This result is in accordance with that reported by Khain et al. (2011) and can be attributed to the fact that in midlatitude storms with strong updrafts, warm rain does not contribute substantially to the total precipitation, so most of the mass of liquid condensate freezes in one way or another. A comparatively weak sensitivity of storm dynamics to aerosols indicates that the difference in hail size, mass, precipitation, and other properties of the storm are largely the consequence of differences in the rates of microphysical processes.

The CCN effects on cloud microphysics are illustrated in Fig. 3, which shows vertical profiles of maximum

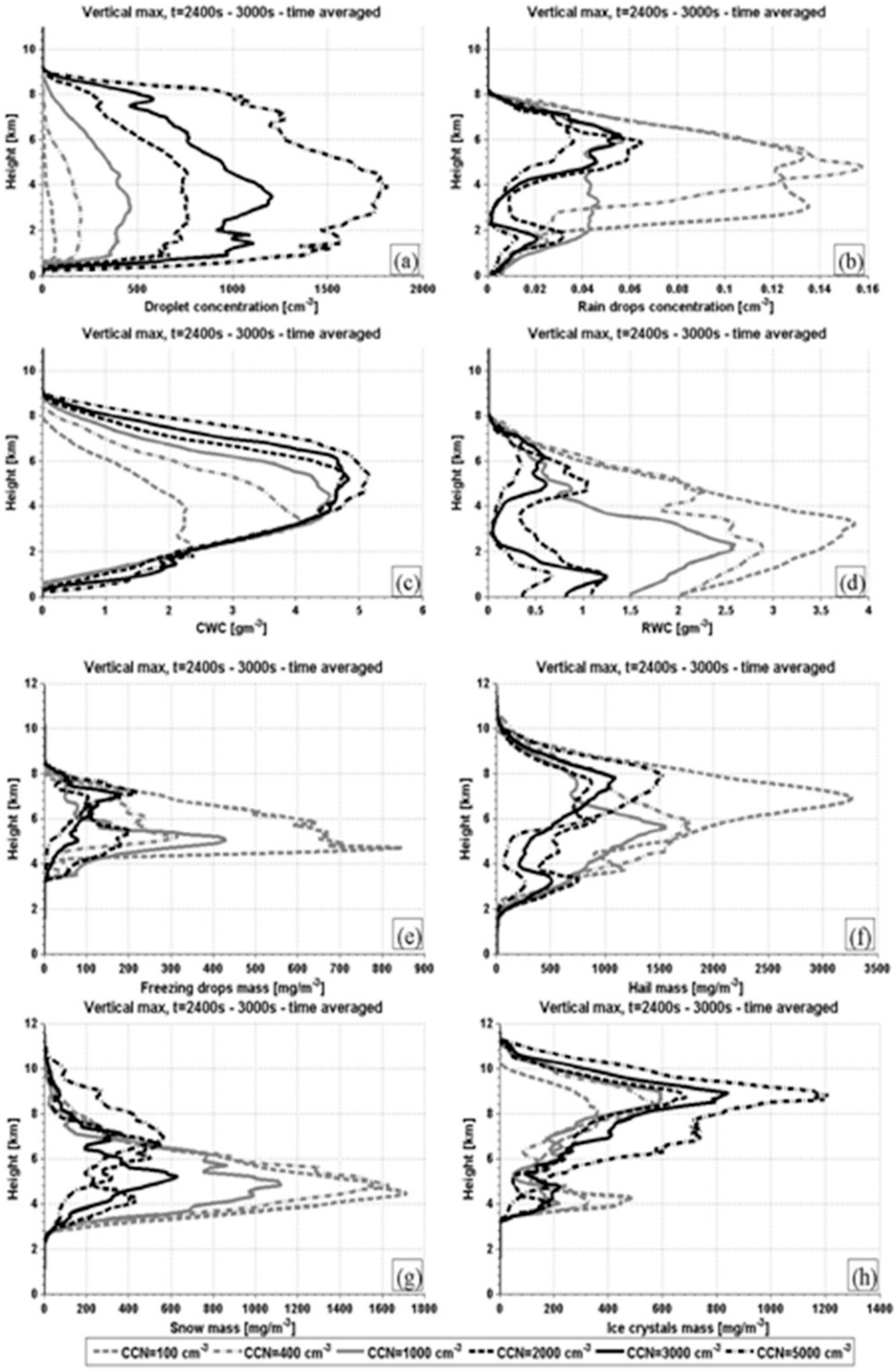

FIG. 3. Vertical profiles of maximum values of (a) droplet concentration, (b) raindrop concentration, (c) cloud water content (CWC), and (d) rainwater content (RWC), as well as mass contents of (e) freeing drops, (f) hail, (g) snow, and (h) ice crystals at the developing stage of storm (deep convective cell). These are shown for different CCN concentrations by the different lines from 100 to 5000 cm^{-3}. The profiles are obtained by averaging over the time period of 2400–3000 s.

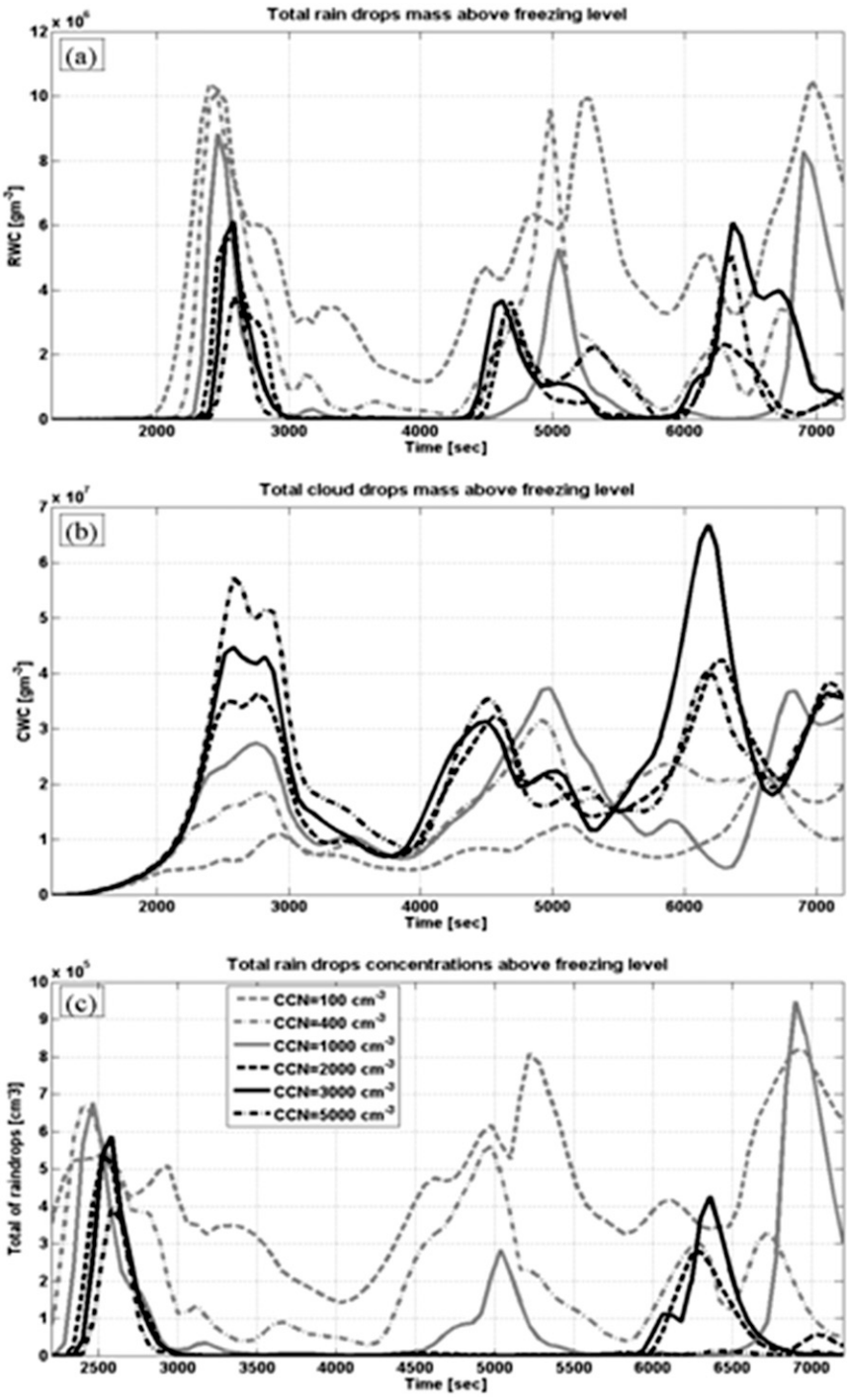

FIG. 4. Time dependencies of (a) total mass of raindrops, (b) total supercooled CWC, and (c) raindrop concentration in simulations with different aerosol concentrations above freezing level shown by the different lines from 100 to 5000 cm^{-3}.

values of cloud water content (CWC), rainwater content (RWC), as well as mass contents of freeing drops (FDWC), hail (HWC), snow (SWC), and total ice crystals (IWC) at the developing stage of the storm. Effects of CCN on cloud microphysics and dynamics of mixed-phase deep convective clouds and storms are determined to a large extent by the CCN effect on supercooled CWC. If the CCN concentration is high, droplets are small and

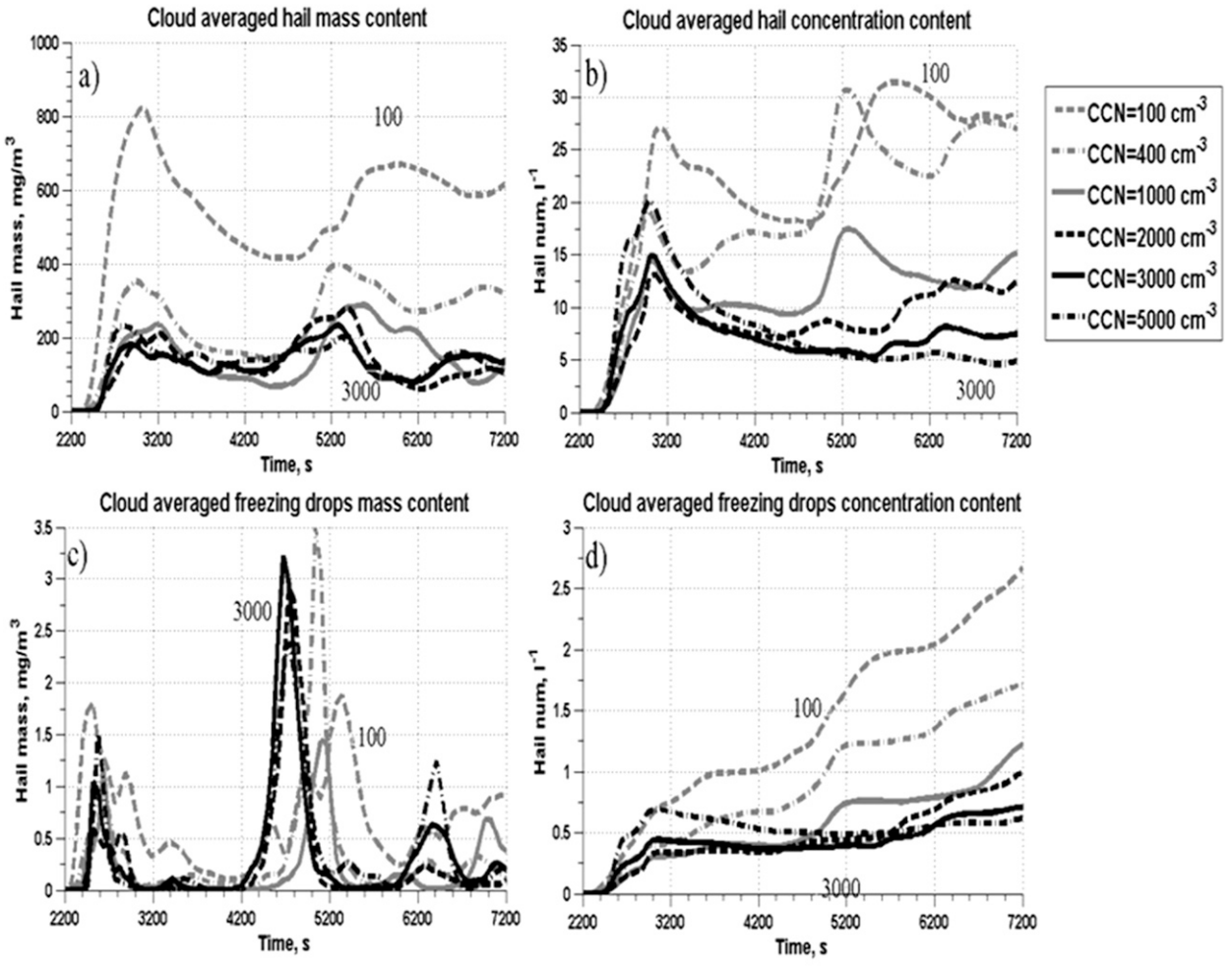

FIG. 5. Time dependencies of cloud-averaged (a) hail mass, (b) hail number concentration, (c) freezing drops mass content, and (d) freezing drops number concentration in simulations with different aerosol concentrations shown by the different lines from 100 to 5000 cm^{-3}. Numbers denote concentrations of CCN corresponding to the particular dependencies.

ascend to high levels (Fig. 3a), forming a significant mass of supercooled water aloft (Fig. 3c). The concentration of raindrops is low (Fig. 3b), the first raindrops form at levels of about 5 km, and the RWC is low (Figs. 5b,d). On the other hand, if the CCN concentration is low, the concentration of cloud droplets is low, but cloud droplets are larger than in cases of high CCN concentration (Fig. 3a). This leads to faster raindrop production and to lower CWC (Fig. 3c), especially as regards the supercooled CWC. As a result, the mass and concentration of raindrops just above the freezing level turns out to be much larger in cases of low CCN concentration (Figs. 3b,c).

These differences in warm microphysics largely determine the difference in the fields of ice particles: 1) Since freezing of raindrops is much more probable than that of cloud droplets, the mass of FDs is larger in cases of low CCN concentration at the developing stage (Fig. 3e). 2) Total freezing of liquid within FDs leads to the production of a significant hail mass content around the altitude of 6 km in cases of low CCN concentration (Fig. 3f). On the other hand, the formation of the first hail in cases of high CCN concentration takes place at higher levels (Fig. 3f). 3) The Hallett and Mossop mechanism leads to formation of ice crystals within the layer with temperatures from −3° to −8°C (altitude range from 4 to 4.8 km) in cases of low CCN concentration (Fig. 3h). Collisions of these crystals lead to snow formation at these levels (Fig. 3g). The lack of FDs, graupel, and hail as well as droplets with diameters exceeding 24 μm at these levels in cases of high CCN concentration makes the Hallett–Mossop mechanism inefficient at the developing stage. In this case, ice crystals form at high levels of 9 km and higher (Fig. 3h).

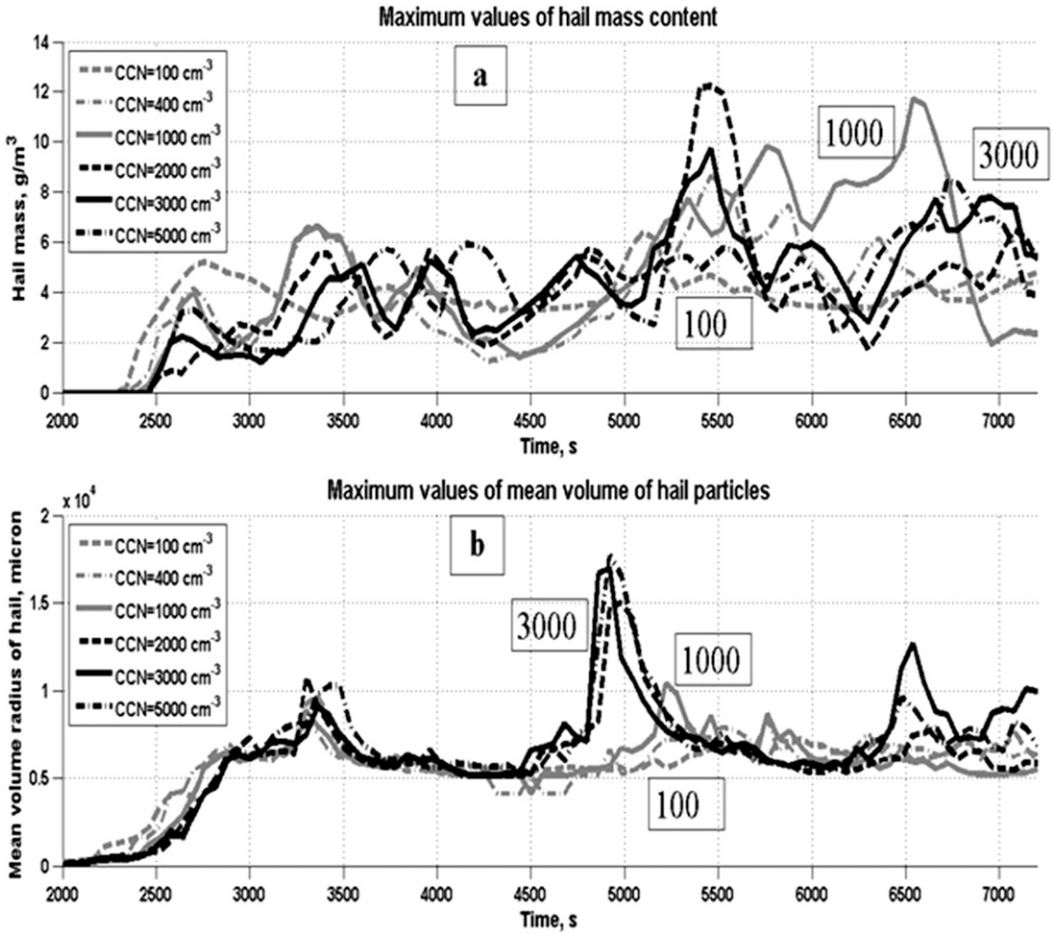

FIG. 6. Time dependencies of maximum mass contents of (a) hail and (b) mean volume radius of hail particles in simulations with different CCN concentrations shown by the different lines from 100 to 5000 cm^{-3}. Numbers in rectangular boxes denote concentrations of CCN corresponding to the particular dependencies.

The rates of production of different hydrometeors and their vertical distributions vary during the storm evolution. However, several basic differences between microphysical structures at different aerosol concentrations are consistent throughout the simulation period. For instance, RWC and raindrop number concentration above the freezing level in cases of low CCN concentration remains larger than in cases of high CCN concentration (Figs. 4a,c), while the supercooled CWC remains larger in cases of high CCN concentration (Fig. 4b) over the entire simulation period.

There are two main mechanisms that determine differences in hail formation at high and low CCN concentrations. In the L_CCN case, the HMC and concentration of hail are determined by a large concentration of raindrops crossing the freezing level. So that the averaged over the cloud volume (cloud average) hail (Figs. 5a,b) and FDs (Figs. 5c,d) mass contents and number concentration in the L_CCN cases are larger than that in H_CCN case. Cloud average values were calculated as ratios of the total mass (or concentration) in grid points within a cloud to the numbers of grid points in which the mass or the concentration were positive.

In high CCN cases, raindrops near the freezing level are small and their concentration is low. The raindrops, FDs and hail in cases of high CCN concentration grow mainly by accretion of these supercooled droplets in cloud updrafts.

Figures 6a,b show time dependencies of maximum mass contents of hail and mean volume radius of hail particles in simulations with different CCN concentrations. One can see that the maximum values of hail mass content, as well and maximum values of mean volume radii, are larger in cases of high CCN concentrations. The maximum hail mass and diameters increase and become substantially larger in high CCN cases at mature stages of convective cells. During this time, the vertical velocities reach their maximal values,

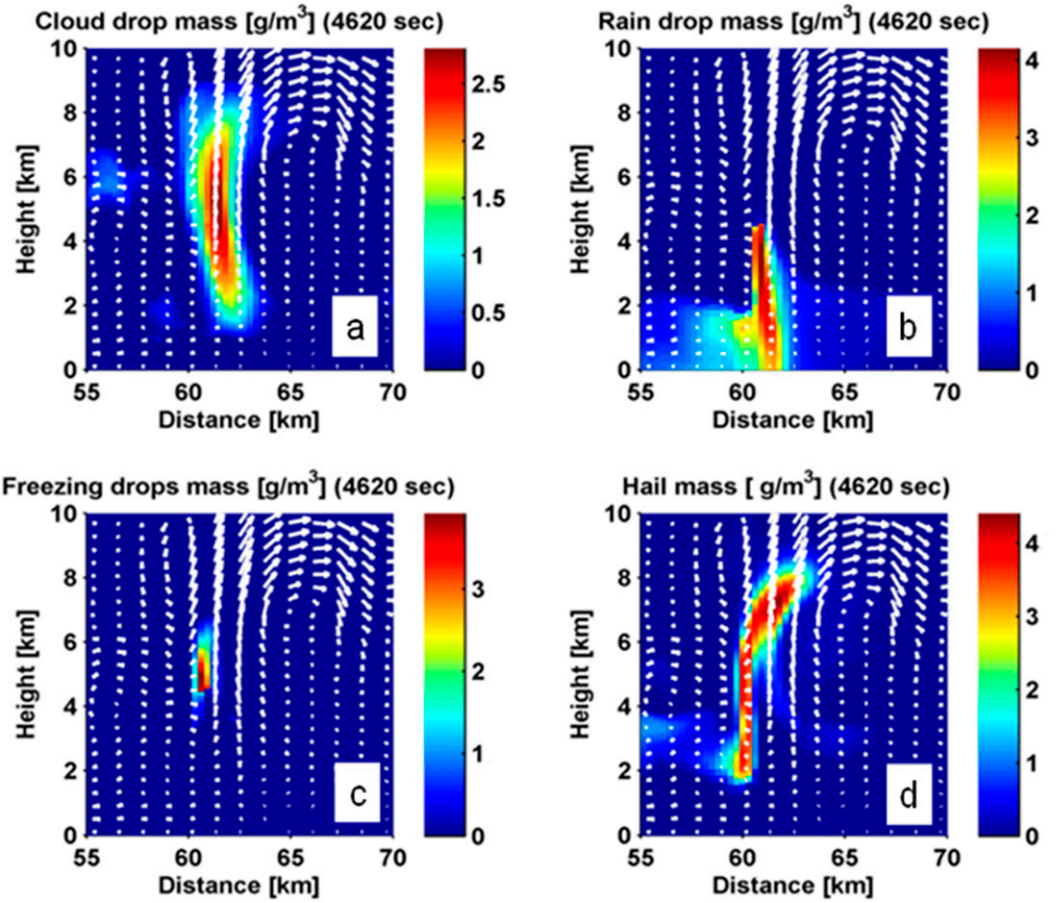

FIG. 7. Height vs distance fields of (a) CWC, (b) RWC, (c) freezing drops mass content, and (d) hail mass in the mature storm (at $t = 4620$ s) in the H_CCN case. The white arrows indicate the background wind fields with the maximum wind vector corresponding to 60 m s^{-1}.

which leads to a corresponding increase in the mass of supercooled droplets and, accordingly, the HMC and hail size aloft.

Thus, despite the larger HMC in cases of low CCN concentration, hail size tends to be larger in the high CCN cases. As will be shown below, the larger hail size in high CCN cases as compared to low CCN cases indicates different mechanisms of hail growth.

b. *Hail and freezing drops in H_CCN case*

A CCN concentration of 3000 cm^{-3} can be considered typical of the high CCN concentration case. The fields of CWC, RWC, mass content of FDs, and hail at the mature stage of the storm are presented in Fig. 7. One can see that cloud droplets ascend in the main updraft (the cloud core) where CWC reaches large values (Fig. 7a). The RWC extends up to altitudes of 4.5 km (~−6°C) (Fig. 7b). Above this level, ice is nucleated inside the raindrops and they are converted to FDs. Significant amounts of FDs extend to about 6-km altitude (~−17°C). Above the altitude of 6.5 km, FDs are converted to hail (Figs. 7c,d). Graupel also contributes to the formation of hail through water drop accretion (see Fig. 1), but its contribution is relatively small (Fig. 24b).

Figure 7 shows that a significant mass of hail and FDs fall along the cloud edge where vertical velocities are much weaker than in the cloud core. The falling hail melts below 2 km, thus increasing the RWC.

Figure 8 shows the field of radar reflectivity, as well as size distribution functions (SDF) of drops, FDs, and hail. SDFs were plotted in two vertical columns: one at $x = 60.3$ km that corresponds to the cloud edge with weak updraft in which maximum hail mass content is located, and the second at $x = 60.9$ km, where the strong updraft (within the core of the cloud) and maximum radar reflectivity took place and at three altitude levels ($z = 3, 4,$ and 5 km).

One can see that radar reflectivity exceeds 50 dBZ up to altitudes of 10 km, which accords with observations (Noppel et al. 2010; Khain et al. 2011). Analysis of the

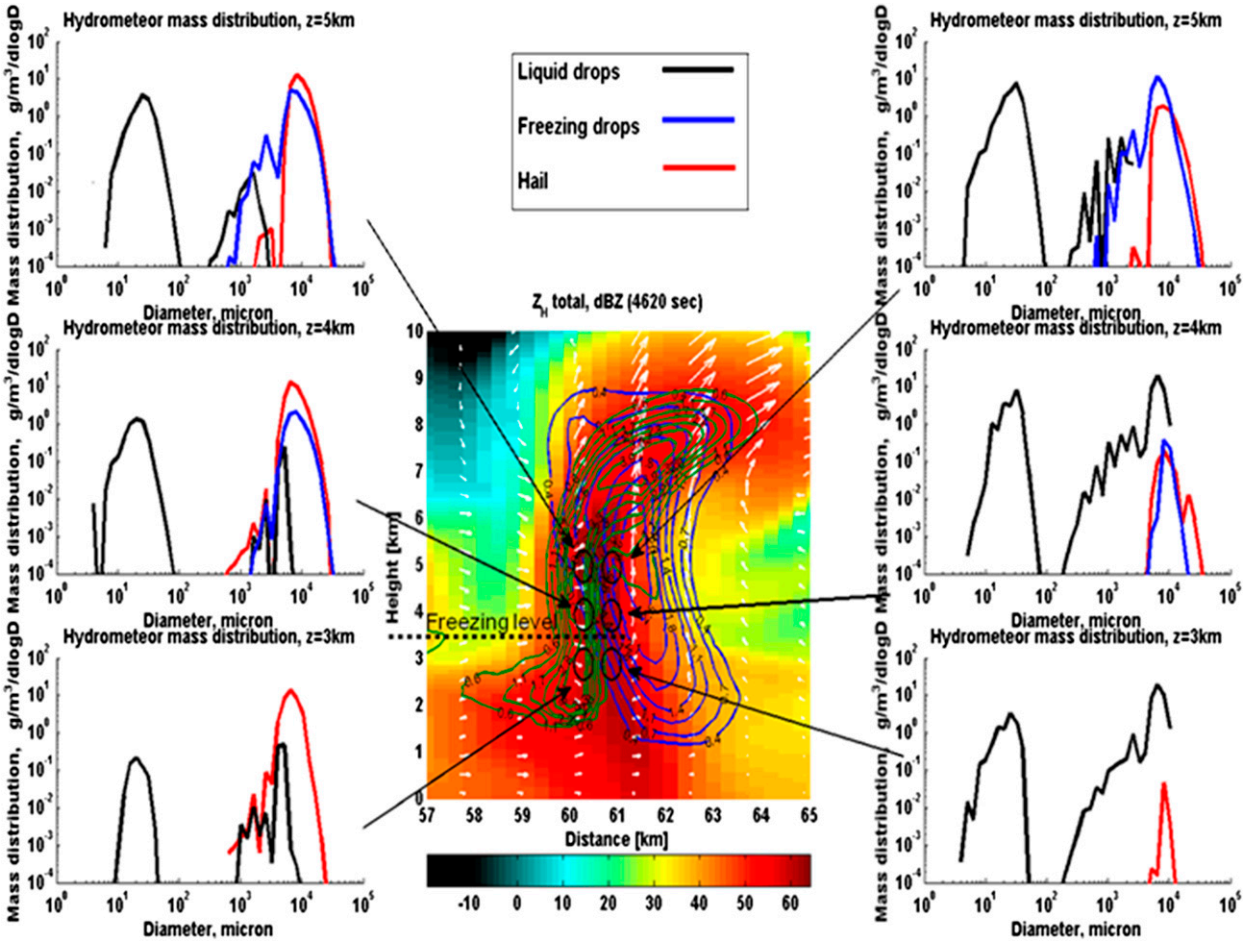

FIG. 8. (center) Radar reflectivity (dBZ). Liquid hydrometeor size distributions (black lines): (left) in the zone of maximum hail mass x = 60.3 km and (right) in the zone of maximum updraft x = 60.9 km at mature stage of the storm, t = 4620 s in the H_CCN case. The arrows and the circles they point to indicate the location of the appropriate size distribution. Overlaid are contours of freezing drops water content (blue) and hail (red) (g m^{-3}).

field of differential reflectivity Z_{DR} (not shown) indicates that Z_{DR} is at a maximum in the zone of updrafts [see Kumjian et al. (2014)]. The question then arises: why is the radar reflectivity high (as well as Z_{DR}) in the cloud updraft of 30 m s^{-1} if the first raindrops in the developing cloud at such high CCN concentration form only at z = 5 km (Khain et al. 2013; Kumjian et al. 2014)?

An analysis of the behavior of SDFs in updrafts and at the cloud edge allows one to answer this question. Let us consider the SDF's evolution in the cloud updraft (Fig. 8, right panels). Note first that in the cloud updraft, the drop size distribution clearly shows the existence of two modes: cloud droplets and raindrops, respectively. A significant mass of large raindrops exists in the updrafts already at an altitude of 3 km in contrast to Fig. 3b (referring to an earlier stage of convection: 2400–3000 s), showing the formation of the first raindrops at an altitude of 5 km. Note also that hail particles with a diameter of 1 cm also exist in updrafts at the 3-km height (Fig. 8). Since above this level vertical velocities are very high, neither raindrops nor hail could fall to this level from above within the vertical column.

An analysis of the SDFs in the updraft at z = 4 and 5 km (with w = 15 and 20 m s^{-1}, respectively) shows that mass contents and the sizes of hail particles and FDs increase upward. At z = 5 km, large raindrops disappear, converting to FDs and then to hail, whose maximum diameter reaches ~3.3 cm.

The behavior of the SDFs at the cloud edge (Fig. 8, left panels) substantially differs from that in the updraft. At z = 5 km, SDFs are quite similar to those in updrafts at the same height level. The only difference is in the larger mass of hail, which is increased both as a result of total freezing of FDs and other mechanisms of hail formation mentioned in Fig. 1. FDs descending along the cloud edge are in the dry growth regime (Fig. 12).

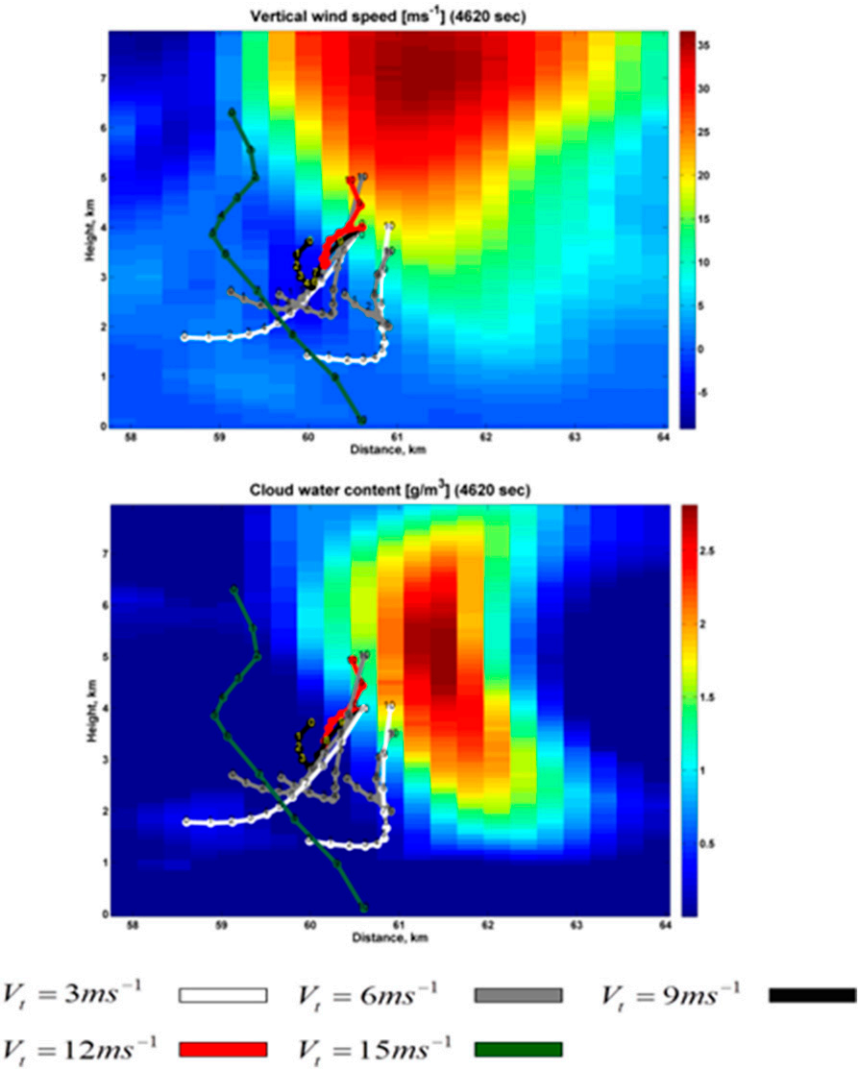

FIG. 9. The fields of (top) vertical velocity (m s^{-1}) and (bottom) cloud water content (g m^{-3}) at $t = 4620$ s corresponding to the mature stage of the storm. These fields are overlaid with 10-min backward trajectories calculated for tracer particles having different (constant) terminal velocities shown by the colors at the bottom. The final points of the trajectories correspond to $t = 4620$ s. The trajectories originate in zones of cloud edges with weak updrafts or downdrafts a few kilometers from the cloud core. The circles on the trajectories indicate the particles' location each minute.

The interior liquid freezes and FDs are converted to hail. As a result, the mass of FDs at 4 km is substantially lower than that at 5 km in this zone. At the level of 4 km, the mass content of FDs is about 10 times less than that of hail (Figs. 12 and 13). Both FDs and hail fall down along the cloud edge and at 3.5 km (melting level) FDs are converted to hail. Shedding from large hail and melting of the smallest hail particles and other ice particles lead to an increase in the RWC. The maximum size of hail falling along cloud edge changes only slightly within the layer between altitudes of 4 and 5 km and slightly decreases downward likely because of shedding.

Comparing the evolution of hail size in updraft and at cloud edge, one can conclude that hail in cases of high CCN concentration grows largely by accretion in cloud updrafts. To clarify how hail, large raindrops, and FDs can appear in the cloud updrafts, we present Fig. 9, which shows the fields of vertical velocity and CWC (right panel) at $t = 4620$ s overlaid with 10-min backward trajectories calculated for ''tracer'' particles having different (constant) terminal velocities. The final points of the trajectories correspond to $t = 4620$ s. The trajectories were plotted for particles with fall velocities from 3 to 15 m s^{-1} with increments of 3 m s^{-1}. The trajectories

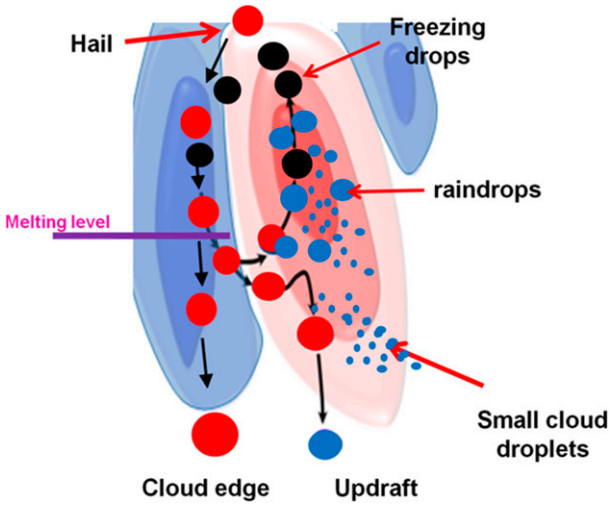

FIG. 10. A conceptual scheme of hail growth in updraft–downward cloud zones at the mature stage of convective cell evolution in case of high CCN (and cloud droplets) concentrations. The scheme corresponds to Fig. 8. The zone of updraft is marked in red; the zone of downdrafts at cloud edge is marked in blue. Notations: small blue circles denote small cloud droplets, large blue circles denote raindrops, black circles denote FDs, and red circles denote hail. See text for details.

originate in zones of cloud edges with weak updrafts or downdrafts a few kilometers from cloud core. The most of trajectories were chosen in such a way as to get the initial points within areas of significant hail water content below melting level. This highlights that even melting hail particles participate in the recycling process when they are involved in the updraft zone. One can see that these particles, reaching their initial location by falling along cloud edges, penetrate the updraft zone where CWC is high and ascend, growing by accretion. The largest particles (with $15\,m\,s^{-1}$) fall to the ground. The conclusion that in cases of high CCN concentration the dominant mechanism of hail growth is accretion in the cloud updrafts is supported by an analysis of the mass budget (see below).

Figure 10 shows a conceptual scheme of hail growth in updraft–downward cloud zones at the mature stage of convective cell evolution corresponding to Fig. 8. The zone of updraft is marked in red; the zone of downdrafts at cloud edge in marked by blue. In updrafts, small droplets (small blue circles) ascend to higher levels. First raindrops are formed at high levels of 5–6 km (large blue circles). After one recirculation, raindrops enter the cloud updraft and turn up within the updraft zone. Raindrops begin freezing, thus producing FDs (black circles). The total freezing of interior liquid within FDs leads to the formation of hail (red circles). Large particles fall along cloud edges and some of them penetrate updrafts and grow in the zone of high CWC (recycling). The largest hail falls down to the surface. Smaller hail melts, producing raindrops. At this stage,

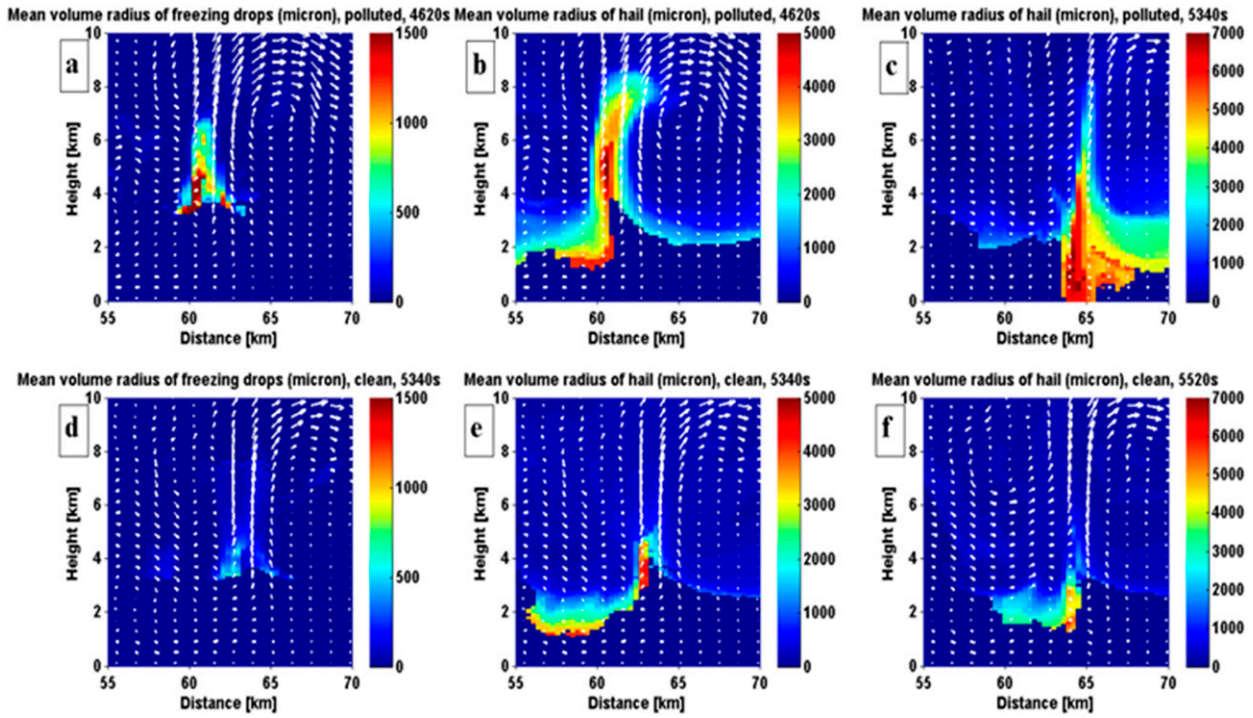

FIG. 11. Height vs distance fields of mean volume radii (μm) of freezing drops and hail in (a)–(c) the H_CNN and (d)–(f) the L_CCN air. Mature stages of convective storm: (left) freezing drops and (center) hail; (right) decaying stage. The white arrows are as in Fig. 7.

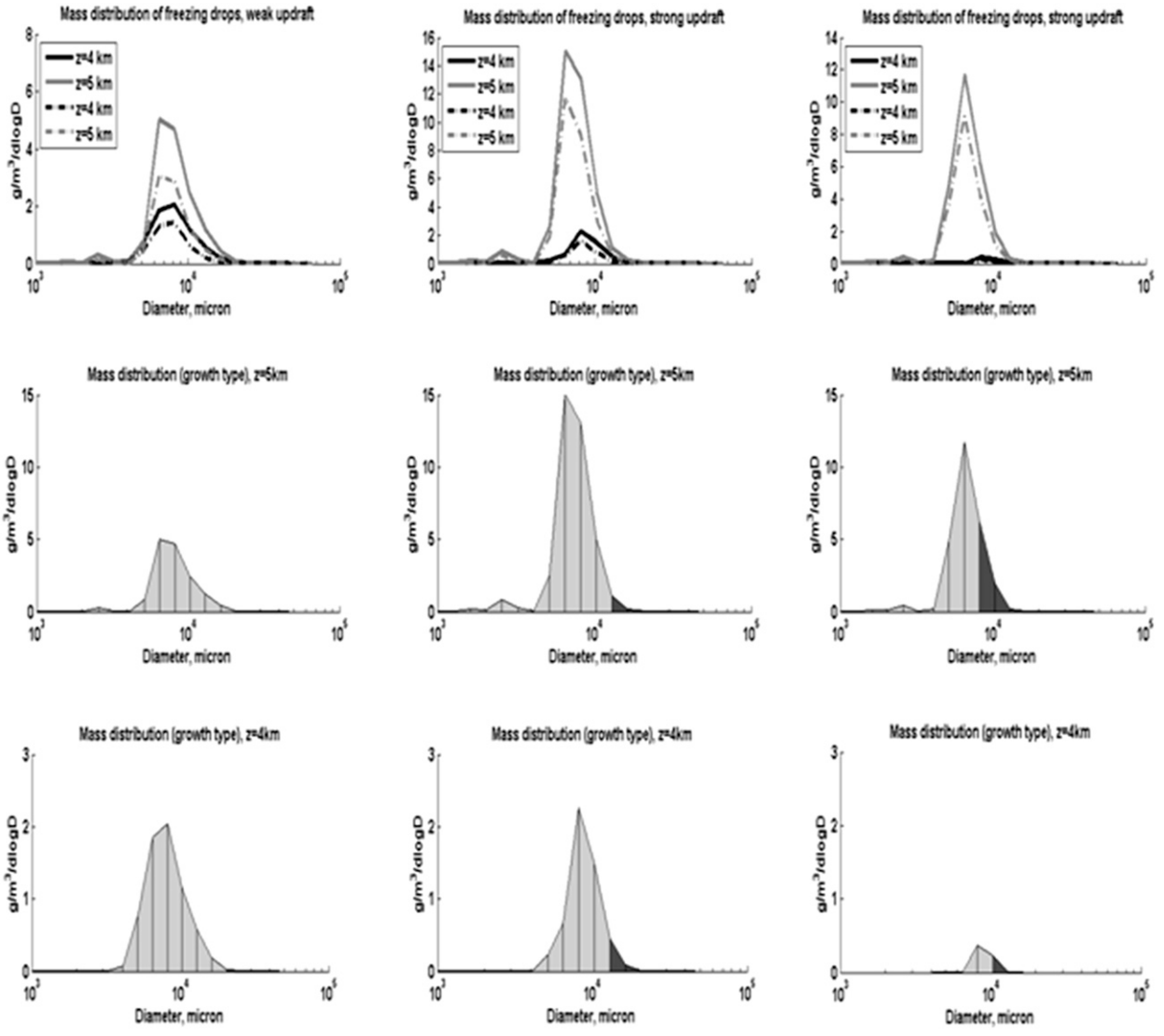

FIG. 12. (top) Mass distributions of freezing drops (entire mass = solid line; liquid water in the particle = dashed–dotted line) at different levels (4 and 5 km) in the vertical columns at (left) $x = 60.3$ km (weak updraft, maximum HWC), (center) $x = 60.6$ km (strong updraft, maximum radar reflectivity), and (right) $x = 60.9$ km (maximum updraft) at the mature stage of the storm ($t = 4620$ s) in the H_CCN case. (middle),(bottom) Mass distributions of freezing drops in which the regimes of growth are marked by light gray are dry and by dark gray are wet growth at 5 and 4 km, respectively; note the differences between the y-axis scales.

hail grows largely during its ascent in updrafts by accretion of supercooled droplets.

Note that during the period of convective cell weakening, hail falls down from above through cloud updraft and grows by accretion (see Fig. 11c). But the appearance of large hailstones aloft that are able to fall down through the updraft is the result of hail growth by recycling. An analysis of Fig. 8 shows that one recycling with a vertical amplitude of 5–6 km takes about 5–7 min. Since the lifespan of a convective cell producing large hail is 15–20 min, the typical number of recyclings is two. This, however, does not exclude cases in which some particles make more recyclings with a smaller amplitude in the vertical.

Figures 11a–c show the fields of the mean volume radius of FDs and hail in the H_CCN case at the mature (4620 s) and decaying (5340 s) stages of convective cell evolution. In the H_CCN case, appreciable masses of FDs (Fig. 11a) and hail (Fig. 11b) with high mean volume radii are concentrated within a relatively narrow zone around the cloud core. Large hailstones form at heights of 5–6 km (Fig. 11b). Hail particles of smaller size continue ascending up to an altitude of 9 km (Fig. 11b). The maximum mean volume radius of FDs is

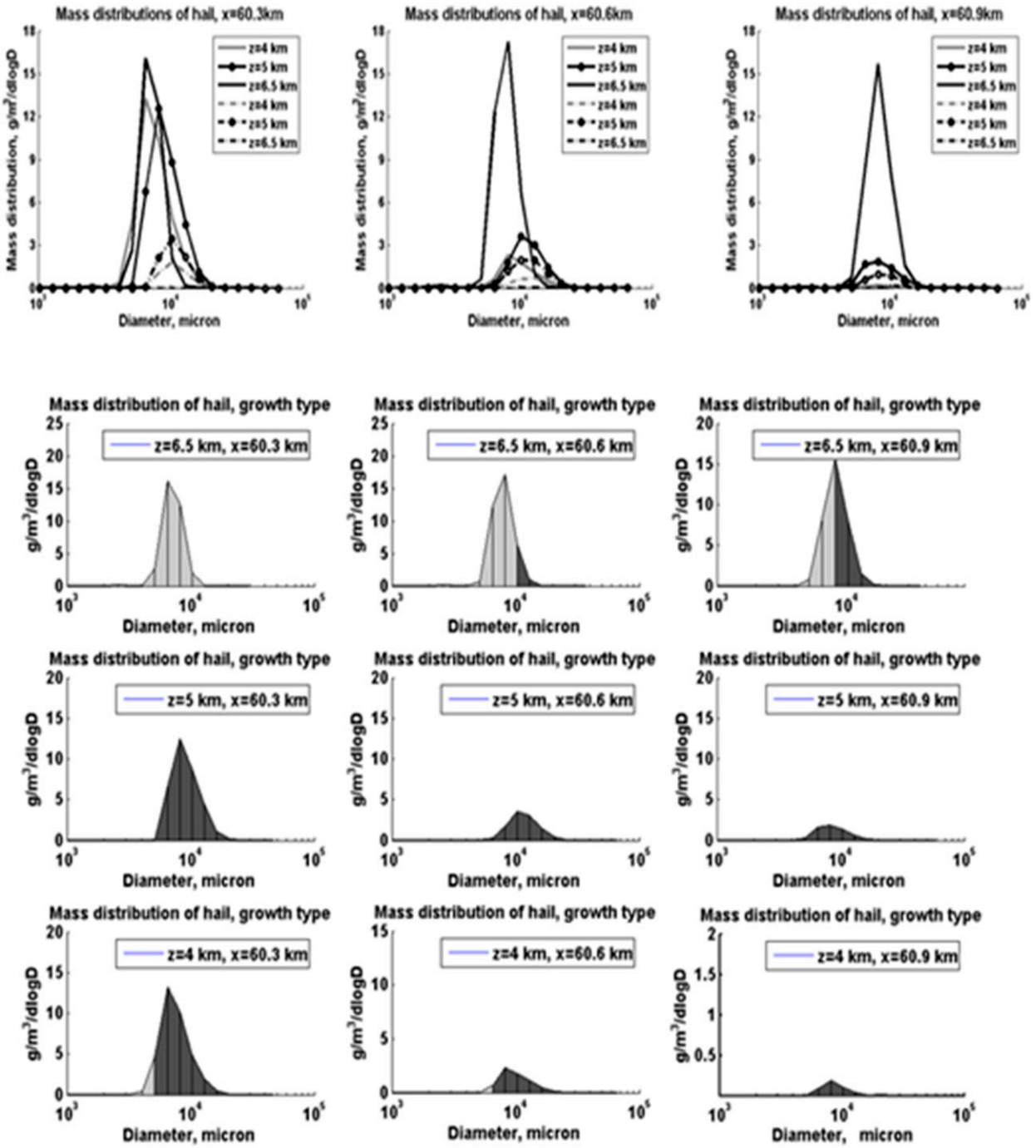

FIG. 13. As in Fig. 12, but for (top) hail at 4, 5, and 6.5 km and with (remaining rows) showing mass distributions of hail at 6.5, 5, and 4 km, respectively.

reached at the cloud edge at relatively low altitudes of 4–4.5 km (Fig. 11a). Analysis of SDF of FDs and hail in Fig. 8 shows that the full freezing of small FDs causes them to be reclassified as hail, thus leaving only the larger drops still present in the ''freezing drops'' category, such that the mean volume radius increases. At the decaying stage (5340 s), hail falls to the surface through the cloud (Fig. 11c). Hail size increases downward.

Figures 11d–f show the fields of the mean volume radius of FDs (Fig. 11d) and hail (Fig. 11e) in the L_CCN case at the mature (5340 s) and decaying (5520 s) stages. The mean volume radii of FDs and hail are much lower

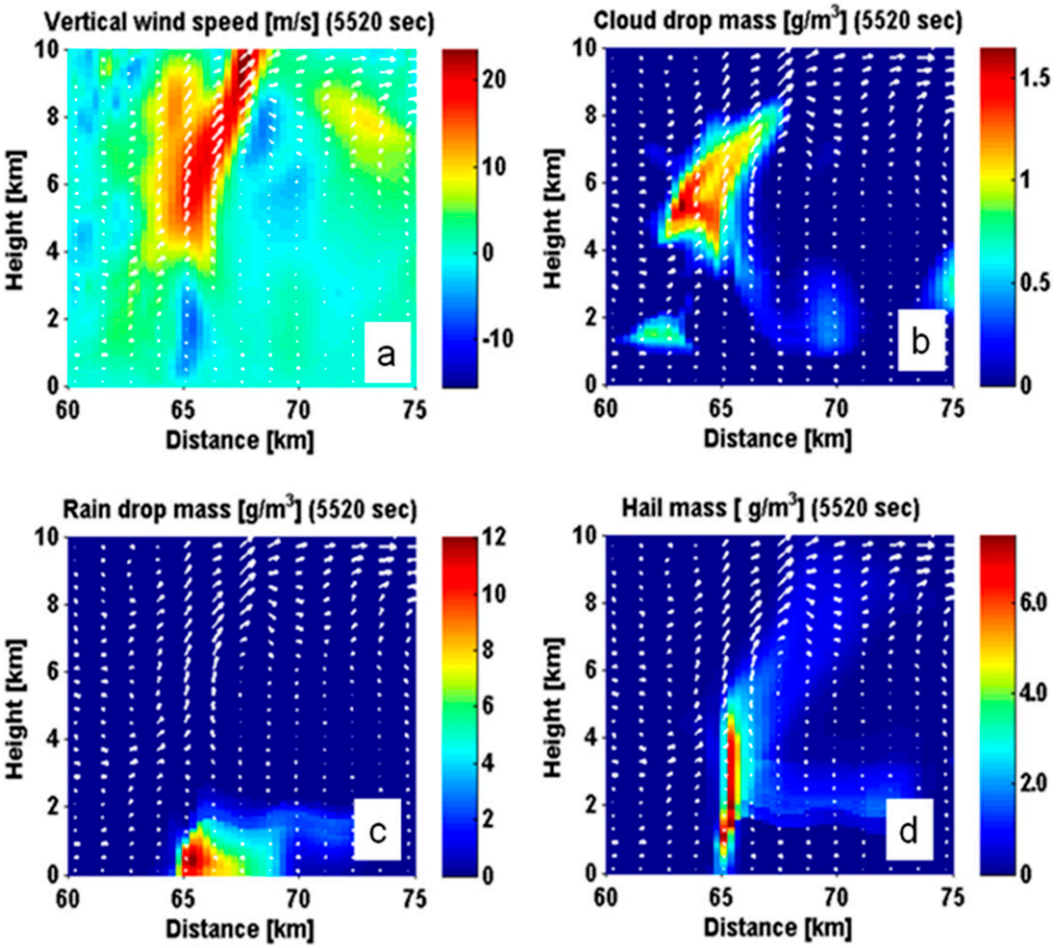

FIG. 14. Fields of (a) vertical wind speed, (b) CWC, (c) RWC, and (d) hail mass at the decaying stage of storm evolution in cases of low CCN concentration. The white arrows are as in Fig. 7.

than the radii in the H_CCN case. In addition, a significant value of the mean volume radius of hail appears only up to 4.5 km. The latter can be attributed to the fact that small amounts of supercooled droplets exist above 4.5 km. Therefore, hail size remains small at the upper levels. Even at the decaying stage (5520 s), hail particles do not reach the ground because of melting (Fig. 11f). The hail remains small, as compared to the H_CCN case. Figure 12 shows the mass distributions of FDs in H_CCN air at altitudes of 4 and 5 km in three columns: $x = 60.3$ km with weak updrafts and downdraft at the cloud edge, $x = 60.6$ km with maximum HMC and radar reflectivity, and $x = 60.9$ km where the updraft was maximum. The figure shows the type of growth regime that was determined according to the presence/absence of exterior liquid. The mass distribution functions of FDs grow upward, especially in zones of high CWC. The largest FDs grow in the wet growth regime in updrafts in the vicinity of the freezing level. At higher levels, exterior water freezes, and above approximately 5 km FDs of all size grow by dry growth (not shown). In downdrafts, the CWC is lower, and the effect of drop accretion on freezing is low. As a result, all FDs grow by dry growth in downdrafts.

Figure 13 shows the mass distributions of hail for the same grid points as in Fig. 12. One can see that the wet growth regime is more common for hail than for FDs. Indeed, dry growth at all hail sizes takes place only in the zone of downdrafts (6.5 km, $x = 60.3$ km) where the environmental temperature is low. The higher incidence of wet growth for hail can be explained by the fact that the big hail is larger than FDs and hail fall velocity is larger than FDs fall velocity, and accordingly, the accretion rate of hail is higher than that of FDs. Another reason is the utilization of different critical surface temperatures determining the wet growth of FDs and hail. According to laboratory observations, the critical surface temperature of hail is as low as −3°C. There are no such data for FDs. Analysis of heat exchange

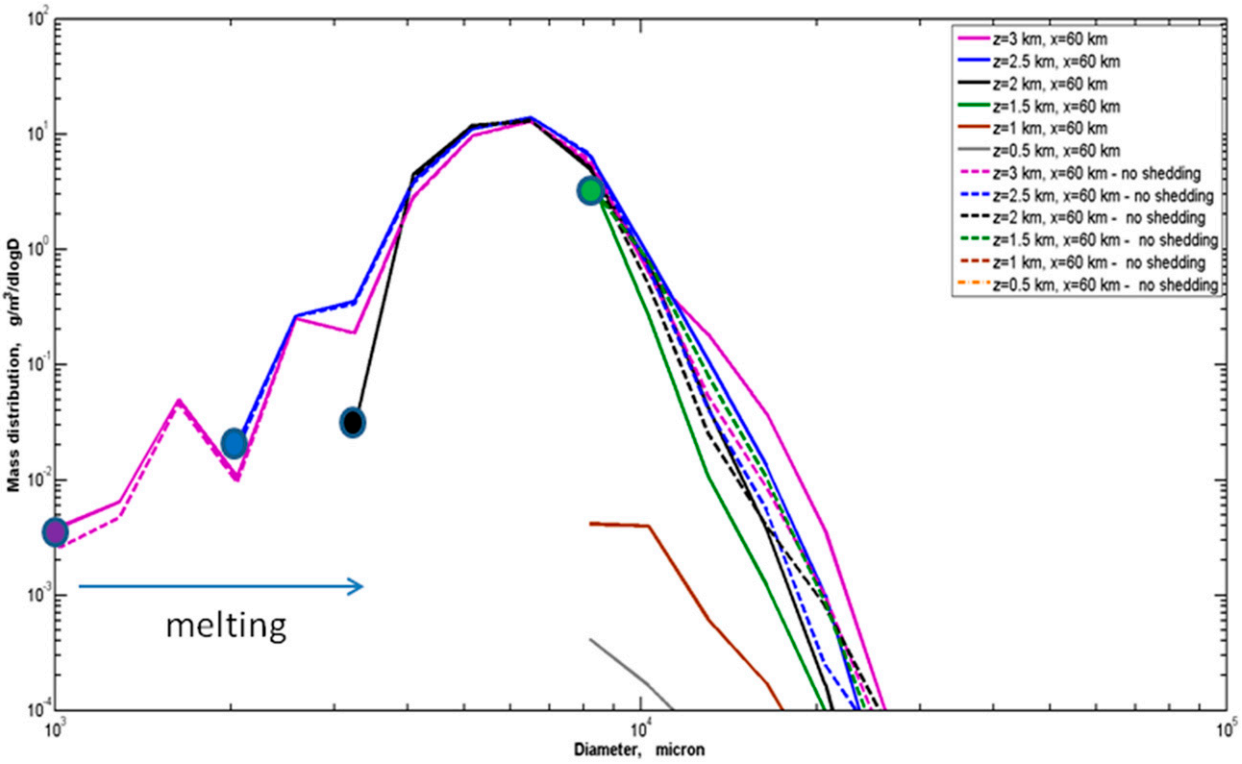

FIG. 15. Mass distributions of hail below the melting level in simulations with the CCN concentration of 3000 cm^{-3} (H_CCN) for x = 60 km. Comparison of simulations with shedding (solid lines) and without shedding (dashed lines) with the color scale running from z = 3 (magenta), 2.5 (blue), 2 (black), 1.5 (green), 1 (brown), and 0.5 km (gray for shedding and orange for no shedding).

equation at the surface of falling particles shows that the critical temperature substantially depends on the assumed surface roughness and should be closer to 0°C for smooth FDs than for rougher hail surfaces. In this study we assume that the critical surface temperature of FDs that wet growth of an FD starts is equal to 0°C. Figure 13 shows that in the strong updrafts the largest hail particles grow in a wet growth regime, at least up to 6.5 km. Below 4.5 km, hail grows by wet growth because of a comparatively high environmental temperature. At z = 4.5 km, wet growth begins for particles larger than 0.5 cm in diameter. At 6.5 km, wet growth begins for hail with a diameter of 0.8 cm. Despite complicated trajectories of hail particles, which are different for different sizes, the mass distributions typically reveal only one boundary size [known as the ''Schumann–Ludlam limit'' (SLL)] separating regimes of hail growth. Hence, the hail-size distribution can be separated into two parts. The particles smaller than the SLL grow in a dry growth regime, while the larger hail grows in a wet growth regime. The SSL depends on environmental temperature and CWC. The regime of wet growth begins when hail is surrounded by a large mass of supercooled droplets. At low altitudes, supercooled water content is larger and temperature is higher. Accordingly, the SSL decreases. The upper row in Fig. 13 shows that liquid water exists only in the largest hail—those with diameters exceeding 0.8 cm. An analysis of the distributions of liquid water and the sizes of hail growing by wet growth shows that there are hail particles that contain interior water but grow by dry growth. This liquid exists within the sponge layer of hailstones (Phillips et al. 2014, 2015).

At the mature stage (4620 s) when vertical velocity reaches is maximum of 40 m s^{-1}, hail falls along the cloud edge, where CWC is relatively small. As a result, hail grows while ascending in cloud updrafts and does not reach to extremely large sizes. Figure 14 shows fields of vertical velocities, CWC, RWC, and hail mass content at the decaying stage of the convective cell (t = 5520 s). As soon as vertical velocity decreases to about 20 m s^{-1} above the altitude of 4 km, and the zone of downdraft forms below the updraft, the recycling is no longer efficient. Hail formed above falls to the surface through the cloud, collecting small droplets. At this stage, hail reaches its maximum sizes.

Below the freezing level, hail particles of smaller sizes fully melt, while the size of large particles changes as a result of shedding and accretion. The RWC forms below

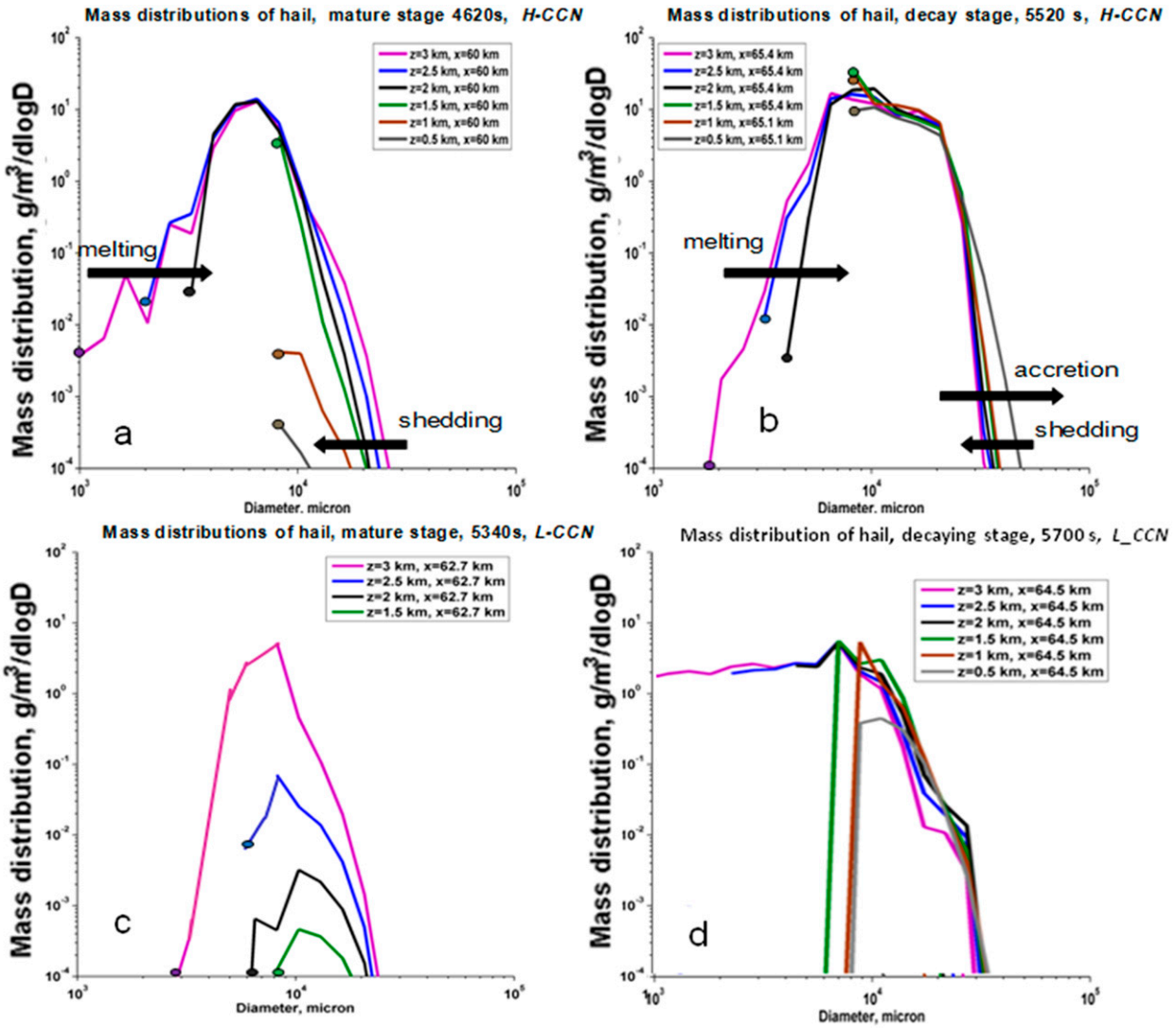

FIG. 16. Mass distributions of hail below the melting level in simulations (top) with a CCN concentration of 3000 cm^{-3} (H_CCN) and (bottom) with low CCN concentration (L_CCN) at the (a),(c) mature and (b),(d) decay stages of convective cell. Arrows show the direction and intensity of changes of the mass size distributions. Colors vs height as in Fig. 15 (shedding).

the 2-km level as a result of melting of the smaller hail and graupel and shedding of the largest hail.

c. *Effects of melting, shedding, accretion, and size sorting on formation of HDFs*

The effects of shedding are of interest. Figure 15 compares hail mass distributions within a column $x = 60$ km in the simulations with and without shedding at the mature stage of the convective cell development when RWC is large at $z = 4$ km and low at lower levels (Fig. 7b). Full melting leads to an increase in the minimum hail size of the hail mass spectrum, as seen in Fig. 15.

The shedding-induced decrease in the maximum hail size is found below $z = 2$ km. At the same time, the figure points to an interesting effect: the maximum hail size in the simulation with shedding at $z = 3$ km is larger than that without shedding. We interpret this result as follows. While each act of shedding decreases the size of the particular hailstone, the shedding of raindrops from the surface of hail increases the number of collectors (raindrops) above the freezing level. These raindrops grow by accretion and convert first to FDs and then to hail. The collision of hail with raindrops above the freezing level increases the maximum hail size. As will be shown below, shedding does not compensate for the effects of accretion.

Interestingly, according to the model results, intense accretion of liquid water can increase the maximum hail

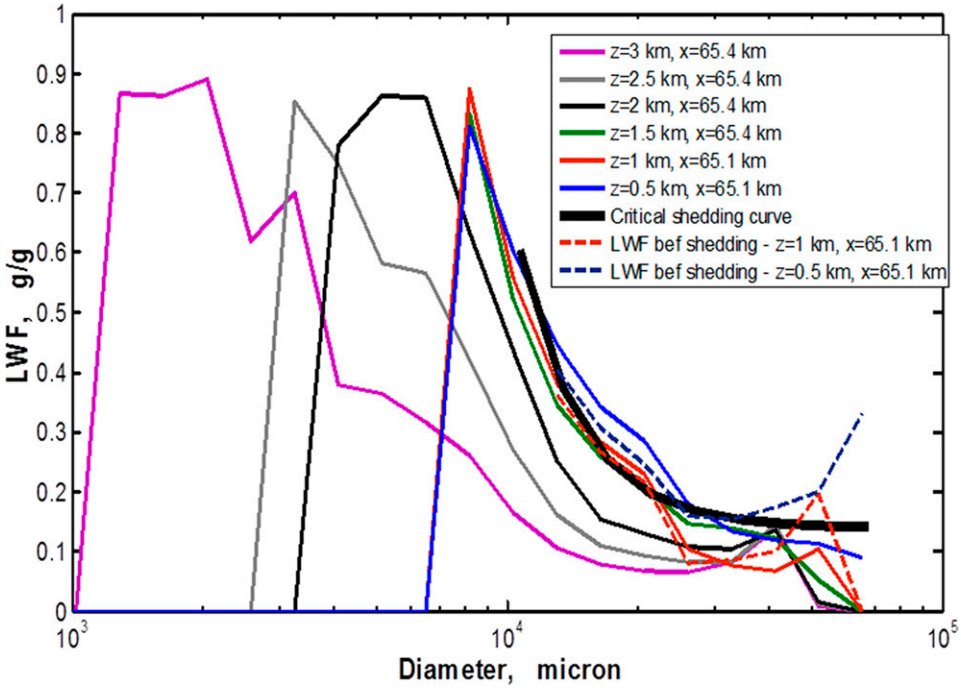

FIG. 17. Distributions of liquid water fraction in hail corresponding to HSDs at the different heights shown in Fig. 16b with $z = 3$ (magenta), 2.5 (gray), 2 (black), 1.5 (green), 1 (red), and 0.5 (blue) km. The black thick line denotes the critical LWF that corresponds to the critical water mass [Eq. (2)]. LWFs before shedding at $z = 0.5$ and 1 km are shown by blue and red dashed lines, respectively.

size even below the melting level. This effect is related to limitations on the shedding imposed by condition (2), according to which shedding takes place only if the mass of liquid water exceeds its critical value. Moreover, according to the condition, the liquid water that remains after shedding should be equal or close to the critical value. Note that this critical value increases with the hail size. Figures 16a,b compares the hail mass distributions below melting level at the mature (maximum updraft, $t = 4620$ s) and the decaying (5520 s) stages in the H-CCN simulation. At the mature stage, hail particles are comparatively small and their melting leads to the appearance of a water mass exceeding the critical value. Moreover, the accretion of liquid water at $T > 0$°C was negligible because of low RWC at $x = 60$ km in the zone of the hail shaft (Fig. 7). As a result, shedding is efficient and the maximum hail size decreases toward the surface (Figs. 15 and 16a). Near the surface, the hail diameter becomes close to 1 cm. For hail of smaller size, it is assumed that shedding does not occur (Rasmussen and Heymsfield 1987). At the decaying stage (Fig. 16b), the hail size increases downward and reaches its maximum of 5 cm near the surface. This size accords well with that observed in the real hailstorm.

Two plausible mechanisms for the increase of hail size toward the surface can be assumed (see Figs. 17–20**)**. Figure 17 shows the distributions of the LWF in hail corresponding to hail-size distributions shown in Fig. 16b. As expected, the LWF increases as a result of melting with a decrease in the altitude. More interesting is that the LWF rapidly decreases with an increase in hail size. This is an expected result because larger hail falls faster than particles of smaller size. A high fall velocity implies a reduction of the residential (melting) time within the layer with $T > 0$°C and a relatively low rate of melting. An analysis of the changes of hail-size distributions (HSDs) indicates that the LWF of large hail increases with accretion because large hail particles fall through the area with high values of RWC (Fig. 18).

Note that not all the accreted and melted water can be shed. In Fig. 17, the black, thick line shows the critical LWF that corresponds to the critical water mass [Eq. (2)]. At levels $z = 0.5$ and $z = 1$ km, the LWF is shown before the shedding procedure at this time step and after shedding (and some other microphysical processes at this time step). One can see that the LWF for the largest hail turns out only slightly higher than the critical value, but after shedding, the LWF is below this curve. Figure 19 shows that shedding does not take place for hail particles smaller than ~0.8 cm in diameter. Following Phillips et al. (2007), we limit the mass of shed water by 50% of the critical mass. Thus, shedding did not decrease significantly

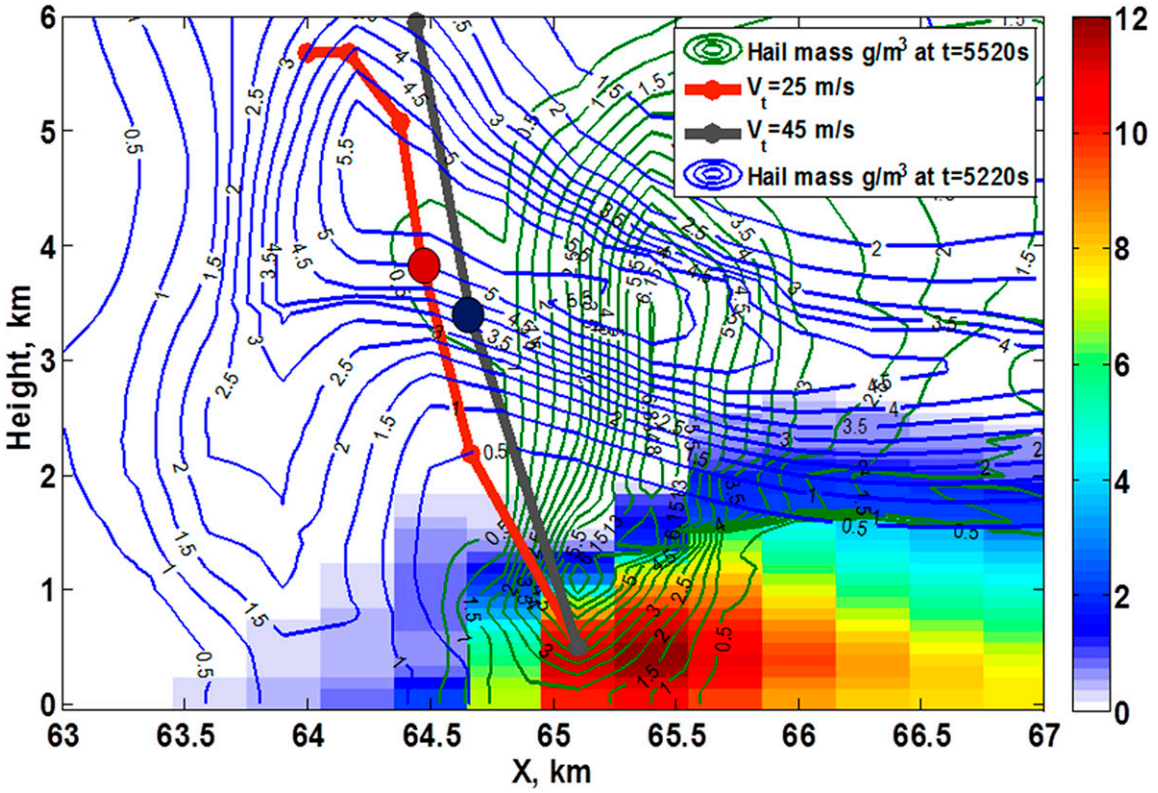

FIG. 18. Field of RWC (color shading, g m^{-3}) in the H_CCN case; this field is overlaid with 5-min backward trajectories calculated for tracer particles with terminal velocities of 25 (red line) and 45 m s^{-1} (black line). The final point of the trajectories corresponds to z = 0.5 km and x = 65.1 km at t = 5520 s. The contours in blue and in green show the hail mass content (g m^{-3}) at t = 5220 and t = 5520 s, respectively. The circles on the trajectories denote the location of particles each minute. The large circles denote the locations where HDFs are plotted in Fig. 20.

the size of large hail particles and in the presence of intense accretion hail size can increase within the melting layer. It is clear that the validity of this conclusion is closely related to the validity of empirical Eq. (2), which is applied here for all hail sizes. To the extent the Rasmussen and Heymsfield curve is valid (or any critical water fraction curve, for that matter), once this critical fraction is reached for a certain hailstone size, no further growth of the hailstone is possible below the melting level.

If the formula is invalid for large hail, and all water is shed from the largest hail particles, the hail size should decrease toward the surface, as in Fig. 16a. At the same time, the decrease in size should be minimal because of the high fall velocity of large hail and the lack of melting time.

Another possible cause of the appearance of very large hail near the surface within a vertical atmospheric column is the size sorting of particles falling within a sheared flow (Kumjian and Ryzhkov 2012). In the presence of sheared flow, hail particles of different size fall along different trajectories. This means that hail particles of different sizes falling at the same point at the surface came from different points of a cloud with different hail size. Two examples of such trajectories are plotted in Fig. 18 for particles with fall velocities of 25 and 45 m s^{-1}. Figure 18 shows also the field of RWC at 5520 s and two sets of contours of hail mass contents for time instances corresponding to the beginning and end of the trajectories. It can be seen that hail falls in the boundary layer through a zone with high RWC. The backward trajectories turned out to be different, so the HSD in the final point of interest is formed by particles following from different locations. Figure 20 shows HSDs in the points marked by large circles in Fig. 18. One can see that the HSD of hail falling along the black trajectory in Fig. 18 is wider and contains larger hail than the HSD of hail falling along the red trajectory. Thus, it also quite possible that the appearance of large hail at lower levels within the melting layer is caused by the size sorting. It is necessary to add that there are several mechanisms of size sorting (Kumjian and Ryzhkov 2012; Dawson et al. 2015). The simple ''transient'' mechanism can also contribute to the formation of hail-size distribution during the decaying stage. Namely, as the updraft

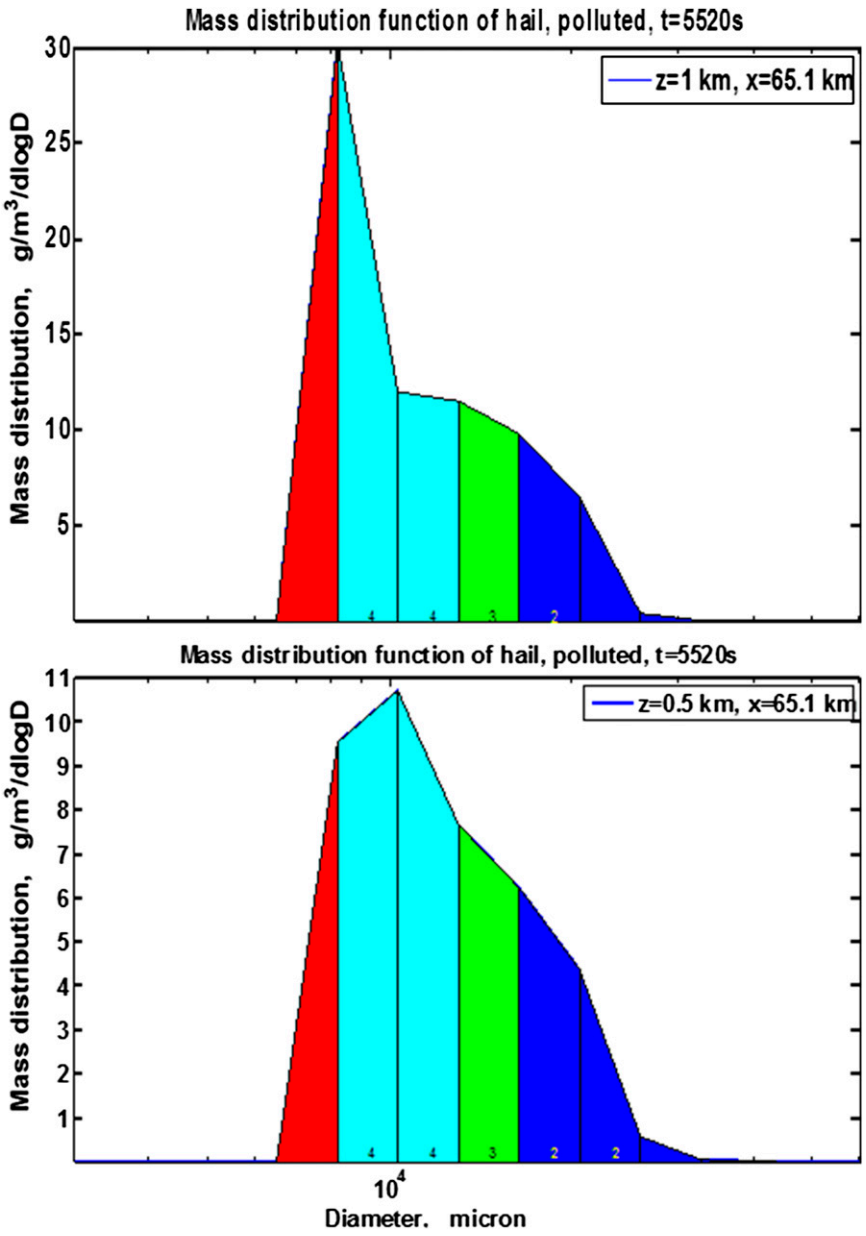

FIG. 19. HSDs in points for $x = 65.1$ km and $z =$ (top) 1 and (bottom) 0.5 km in the H_CCN case. Colors show the mode of shedding (2—blue: Re > 15 000, 3—green: 15 000 > Re > 10 000, and 4—pale blue: Re < 10 000; see text for details). No shedding is marked in red.

that originally held the hail in suspension decays, a transient ''pulse'' of hail descends toward the ground. The larger hailstones outrun the smaller ones and, thus, reach the low levels first. At any given snapshot in time, especially one taken just as the leading edge of the hail pulse is nearing the surface, will show larger hailstones near the bottom and smaller ones near the top.

We suggest, therefore, that both accretion and size sorting contributed to the formation of the HSD in the BL at the decaying stage.

The analysis shows that all the shedding modes found by Rasmussen et al. (1984) in laboratory experiments are realized in the model. Figure 19 shows HSDs for $x = 65.1$ km and $z = 1$ and 0.5 km. The colors show the mode of shedding according to the particle's Reynolds number: 2—blue for Re >15 000, 3—green for 15 000 > Re >10 000, and 4—pale blue for Re < 10 000. No shedding is marked in red. As can be seen, shedding takes place for hail with diameters above 0.8 cm. For Re > 25 000, all exterior meltwater is shed

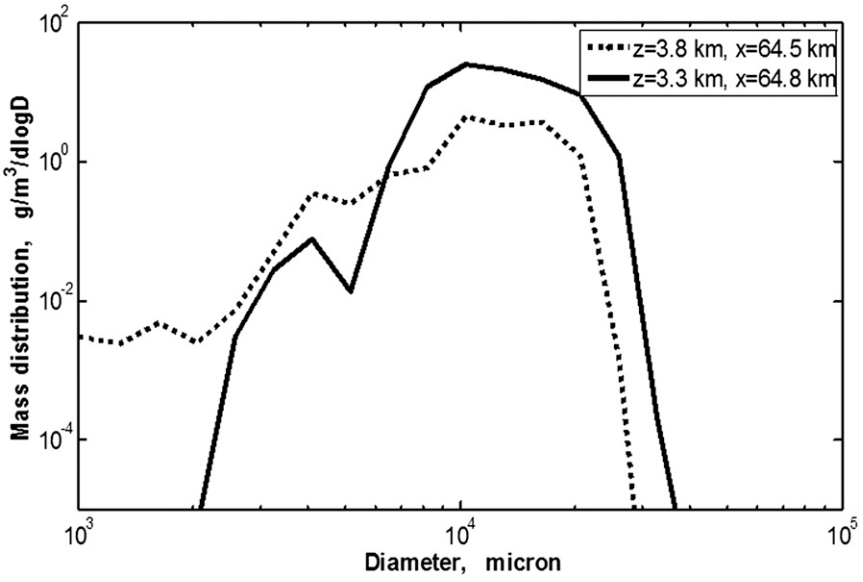

FIG. 20. The hail-size distributions in the points marked by large circles in Fig. 18. Solid line corresponds to black circle; dashed line corresponds to red circle.

discontinuously as a burst of raindrops of 1.5 mm in diameter when its mass exceeds the critical threshold. For 15 000 < Re < 25 000, there is continuous shedding of such raindrops and the mass of exterior liquid is maintained at the critical equilibrium value (in Fig. 19, mode 2—blue). For Re < 15 000, there is intermittent shedding of raindrops of 3 mm (Re >10 000—in Fig. 19, mode 3—green) or 4.5 mm (Re < 10 000—in Fig. 19, mode 4—pale blue) in diameter, reducing the mass of exterior meltwater in each shedding event such that it is less than the critical water mass.

d. *Hail and freezing drops in the L_ CCN case*

Figure 21 shows fields of CWC, RWC, mass content of FDs, and HMC at the mature stage in the L_CCN simulation with a CCN concentration of 100 cm^{-3}. A comparison of the fields in Fig. 16 and 7 shows that the FD mass content in L_CCN is smaller than in corresponding clouds in the H_CCN case and that the FDs totally freeze already at an altitude ~5 km, as compared to 6 km in cases of high CCN concentration. This can be attributed to the relatively weak accretion in L_CCN because of low CWC.

As mentioned above, the number concentrations of FDs and hail particles (see Figs. 5b and 5d) in the L_CCN are much higher than in the H_CCN because a much larger number of comparatively large raindrops are able to freeze in the vicinity of the freezing level in L_CCN. The efficient freezing of raindrops near the freezing level in L_CCN is related not only to the comparatively large size of the raindrops but also to a relatively low updraft velocity, which results in the raindrops spending a significant amount of time before reaching low temperatures. However, the maximum hail size is smaller than in the H_CCN (see Figs. 11b,c and 11e,f) because of a lack of intense accretion. While in the H_CCN case hail is concentrated in the zone of high updrafts (~25 m s^{-1} average maximum values) and CWC (Fig. 7a and Fig. 11b), in the L_CCN a significant fraction of small hail spreads over a large area by being advected by velocity field up to an altitude of 11 km and by 10–15 km in the horizontal direction (Fig. 16d).

Figures 22 and 23 show the mass distribution functions of FDs and hail, respectively, as well as the growth regime of the particles in vertical atmospheric columns where the maximum mass contents of FDs and hail take place. As can be seen in Fig. 22, FDs grow by the wet growth regime only close to the freezing level. At higher levels, FDs grow in the dry growth regime. In the L_CCN case, hail also grows by the wet growth only in the vicinity of freezing level. Above about 4.7 km (~1.2 km above the freezing level), hail grows in dry growth regimes. This altitude is much lower than 6.5–7 km in the H_CCN case. The difference is explained both by the smaller size of hail and the lower CWC in the clean case, resulting in much lower rates of accretion of drops.

Comparison of the mass size distributions of FDs and hail in the L_CCN and H_CCN cases shows the 1) larger size of particles in H_CCN case, as discussed above, and 2) bimodality of the mass size distributions in the L_CCN case as compared to unimodality of the mass

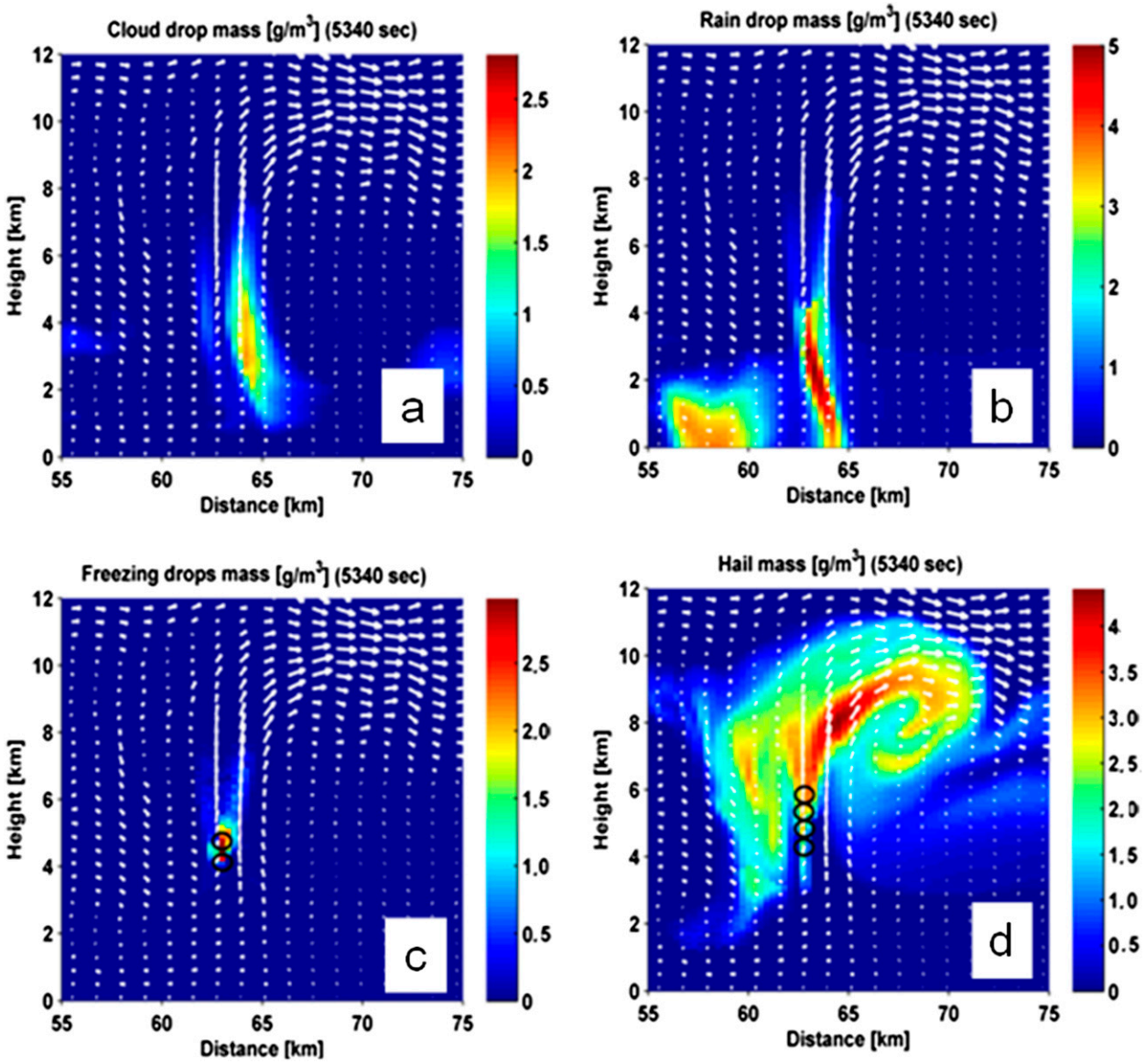

FIG. 21. The FD fields of (a) CWC, (b) RWC, (c) freezing drops mass content, and (d) hail mass in the low-CCN-concentration case at the mature stage of storm evolution. The white arrows are as in Fig. 7. Circles show points in which mass distribution functions are plotted in Figs. 22 and 23.

distribution functions in H_CCN. The reasons for such differences are not well understood and require additional investigation. We attribute this difference in the shapes of the mass size distributions to the following. Because of the highly nonlinear dependence of freezing rates on raindrop size and temperature, only the largest raindrops freeze near the freezing level. This leads to the formation of the first mode in the distribution of FDs in L_CCN at $z = 3.9$ km (Fig. 21a). At higher levels, smaller raindrops start freezing, forming the second mode in the mass distribution of FDs in L_CCN (Fig. 21b). The total freezing of liquid in FDs leads to the formation of bimodal hail distributions in the L_CCN case. As can be seen in Fig. 23 (top three panels), the formation of bimodal hail distributions occurs between 5 and 6 km. At an altitude of 4.5 km, there is no bimodal distribution of hail, since smaller raindrops did not convert to FDs (and accordingly FDs did not convert to hail) at this level and below.

In the H_CCN case, FDs and hail grow by accretion in the course of recycling. Initially, first raindrops form only at 5–5.5 km. The evolution of FDs and hail mass distribution in cloud updrafts under high CCN concentration is shown in Fig. 8 (three mass distributions shown

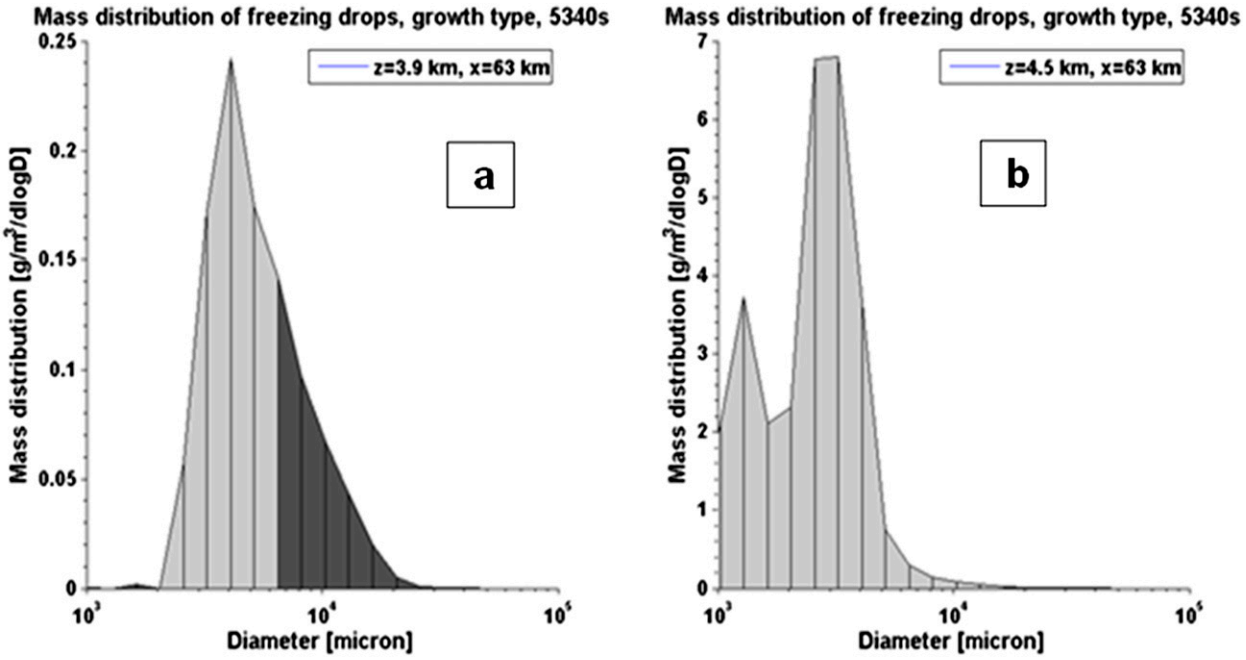

FIG. 22. Mass distributions of freezing drops in the case of low CCN concentration in points shown by circles in Fig. 21c: z = (a) 3.9 and (b) 4.5 km. Dry growth is denoted by light gray and wet growth is denoted by dark gray.

on the right). One can see that the formation of new FDs and hail by the freezing of the largest raindrops takes place at altitudes of about 5 km. This freezing is seen by the disappearance of the largest raindrops in the raindrop mass spectra. Newly formed hail is large, with a comparatively narrow unimodal mass distribution.

Figures 16c,d show the mass distributions of hail at the mature (5340 s) and decaying (5700 s) stage below the melting level in the L_CCN case. The mass of large hail with diameters exceeding 1 cm is much lower than in the H-CCN case. At the mature stage, hail totally melts before reaching the ground. Fast melting fosters the intensification of shedding, thus leading to a decrease in maximum hail size in the downward direction. At the decaying stage, when hail reaches the ground, its mass is about 10 times less than in the H_CCN case.

e. Budget considerations

A comparison of the fields of CWC, FDs, and hail in H_CCN and L_CCN indicates significant differences in the mechanisms of hail formation in these cases and suggests that the main reasons for the differences lie in the warm microphysics leading to lower supercooled CWC and higher raindrop concentration in L_CCN.

Here we analyze the mechanisms of hail formation under different CCN concentrations using mass budgets. Three major processes that contribute to hail mass are riming (accretion of liquid droplets), total freezing of FDs, and the transformation of graupel to hail due to wet growth and according to graupel size (Fig. 1). The main process that decreases hail mass is melting.

Figure 24 presents the time accumulated over the computational area production of hail due to these processes. One can see that riming is the most important component of the mass budget. Figure 23a shows that in H_CCN the main mechanism of hail mass content is accretion, which is stronger than in L_CCN.

The second of the major processes is the conversion of FDs to hail during the full freezing (Fig. 24c). One can see that in L_CCN, this process dominates as regards to the production of new hail. As discussed above, this is explained by the larger mass of comparatively large raindrops that freeze close to the freezing level in L_CCN.

Conversion of graupel to hail due to the accretion of supercooled liquid by graupel is more intense in H_CCN, but this process is less important as compared to accretion and freezing (Fig. 24b). This mechanism is inefficient in the L_CCN case because of low supercooled CWC. Despite the fact that the overall mass of hail is larger in the L_CCN case, the hail downward mass flux at the melting level is larger in the H_CCN case because of larger hail size and larger fall velocities of hail in this case. Figure 24d shows that melting is more intense in the H_CCN case, which can be attributed to the fact that larger hail mass falls to warmer lower levels (near the ground), thus enhancing the melting rates. In contrast, the smaller hail in L_CCN melts higher up before reaching the ground. Despite the more intense

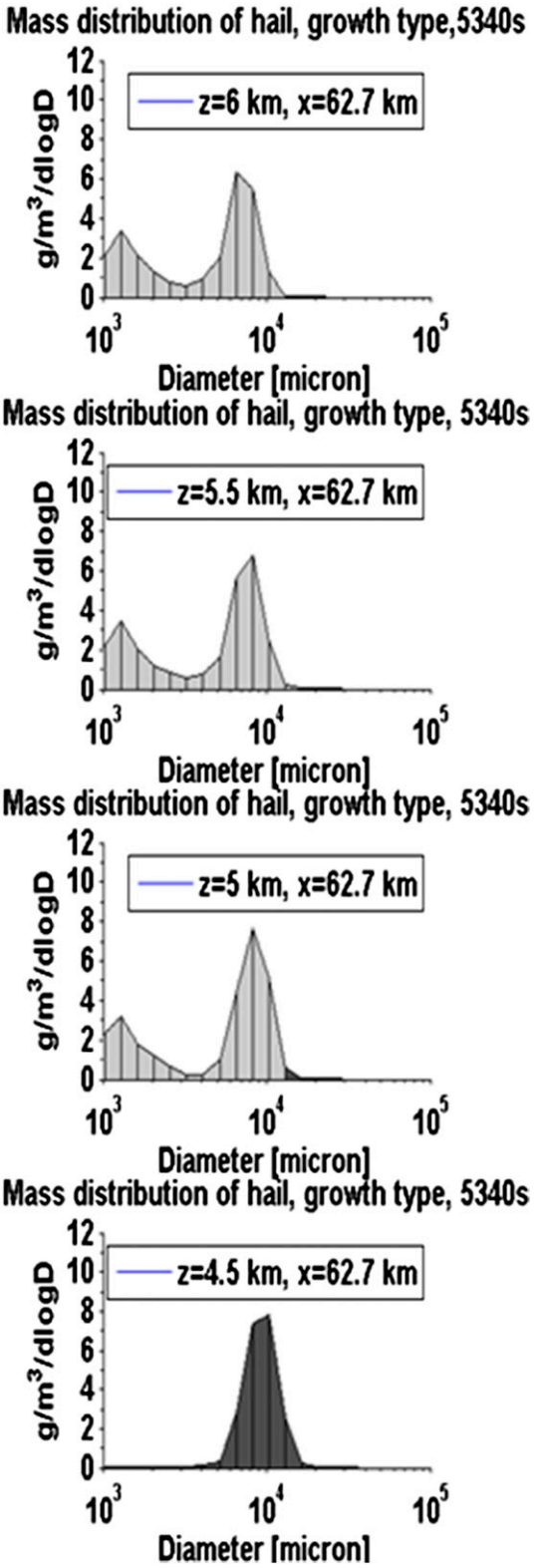

FIG. 23. Mass distributions of hail at the mature stage of convective cell in the case of low CCN concentration in points shown in Fig. 21d by circles: (top to bottom) $z = 6$, 5.5, 5, and 4.5 km. Dry growth is denoted by light gray and wet growth is denoted by dark gray.

melting in the H_CCN case, the larger hail size in this case determines much higher surface hail shaft in this simulation.

One of the main components of mass budget in the atmosphere is precipitation. Figure 25 shows time dependencies of accumulated rain at the surface (top panel) and hail precipitation. One can see that before 60 min, rain mass is larger in the L_CCN case, while later on, rain mass is substantially lower than in other simulations. At CCN concentrations exceeding 1000 cm^{-3}, accumulated rain is only slightly sensitive to aerosols. As seen in Fig. 25 (bottom), the maximum hail shaft takes place at a CCN concentration of 3000 cm^{-3}. The low hail shaft in clean-air cases is related to the small sizes of hail and efficient melting. The decrease in the hail shaft at extremely high CCN concentrations (i.e., those larger than 3000 cm^{-3}) can be attributed to the generation of high concentrations of ice crystals in cloud anvils due to homogeneous nucleation of the extremely small droplets (Fig. 26). These ice crystals spread over a large area and do not participate in the process of precipitation formation. Figure 26 shows that the mass of these ice crystals substantially increases when the CCN concentration increases from 3000 to 5000 cm^{-3}. The increase in ice crystal concentration can be attributed to the fact that very small droplets arising under extremely high CCN concentrations cannot be captured by ice crystals and graupel (Pruppacher and Klett 1997; Khain et al. 2001). Consequently, these droplets do not participate in the process of riming.

Figure 27 shows the time dependence of maximum RWC and HMC in the H_CCN and L_CCN cases in simulations with and without shedding above the freezing level. One can see that shedding substantially decreases hail mass and increases RWC at $t > 5000$ s in the H_CCN case, when hail reaches comparatively large sizes, so that shedding becomes possible. Since in the clean-air case (L_CCN), hail size is small, the effects of shedding are negligible as regards effects on the maximum values of RWC and HMC.

f. The shape of hail number concentration distribution functions

The amount of in situ measurements of number distribution functions of hail in deep convective clouds and storms is very limited. Owing to low values of hail concentration, collection of the required data demands that the size distributions of hail particles should be measured along long flight tracks of many tens of kilometers to get the necessary statistics. To get statistically significant hail-size distributions during surface measurements at particular points, the measurements should be performed over a comparatively long period and averaged over

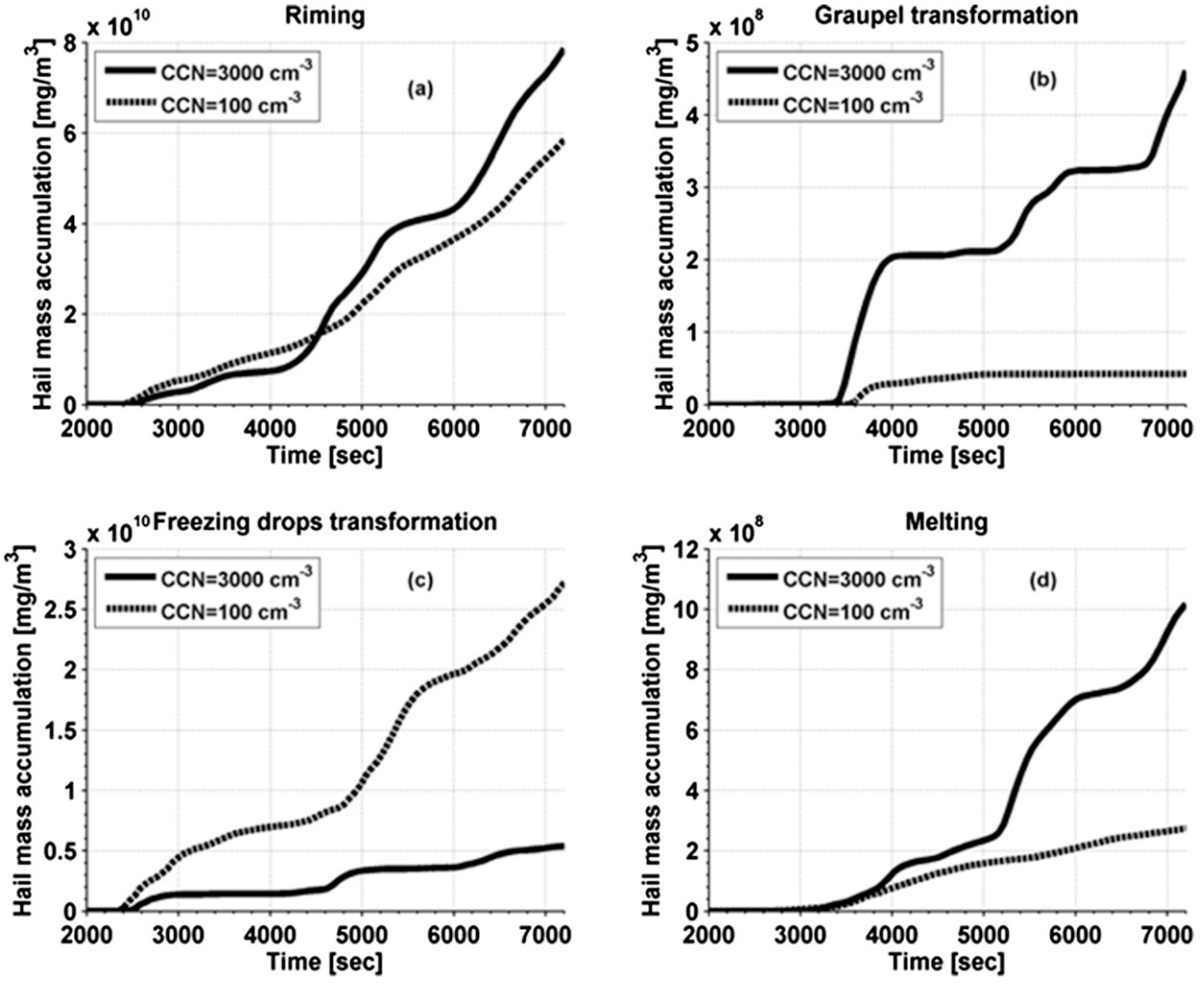

FIG. 24. Hail mass transformation vs time for hail budget items in H_CCN and L_CCN: (a) riming, (b) graupel transformation, (c) freezing drops transformation, and (d) melting for CCN = 3000 (solid black) and 100 (dashed black) cm^{-3}.

many samples (Cheng and English 1983; Cheng et al. 1985). At the same time, hail is obviously distributed nonuniformly over clouds and the sizes of falling hail change with time. Note that the processes of precipitation (including hail shaft) formation are determined by local size distributions, which can substantially differ from those obtained by averaging over a span of time.

Despite the fact that two- and three-moment bulk-parameterization schemes can, in principle, calculate parameters of gamma or exponential size distributions, the data about simulated size distributions under different aerosol conditions and in different zones of clouds are typically absent. A rare exception, Loftus and Cotton (2014b), offers only one example of such a distribution. Hence, number concentration hail distribution functions that are calculated using the SBM cloud models are of interest. Figures 28a,c show hail number concentration distributions below freezing level in simulations H_CCN (left) and L_CCN (right) at different heights, while Figs. 28b,d show distributions at the same altitudes at different horizontal locations. This figure illustrates the hail-size distributions in vertical columns where at these time instances HMC near the surface (top row) was maximum. The HSD are plotted for $z = 1.6$ km (bottom row) in the H_CCN run and at $z = 3.5$ km (bottom row) in the L_CCN run. The horizontal grid points were chosen around the point with maximum HWC at the corresponding levels. The height of 3.5 km in the L_CCN run was chosen because in this case hail particles are small and melt below. The number distributions that most closely resemble the gamma distribution are formed at the decaying stages within a strong hail shaft near the surface in the H-CCN cases (Fig. 28). Horizontally averaged number distribution functions more closely resemble the

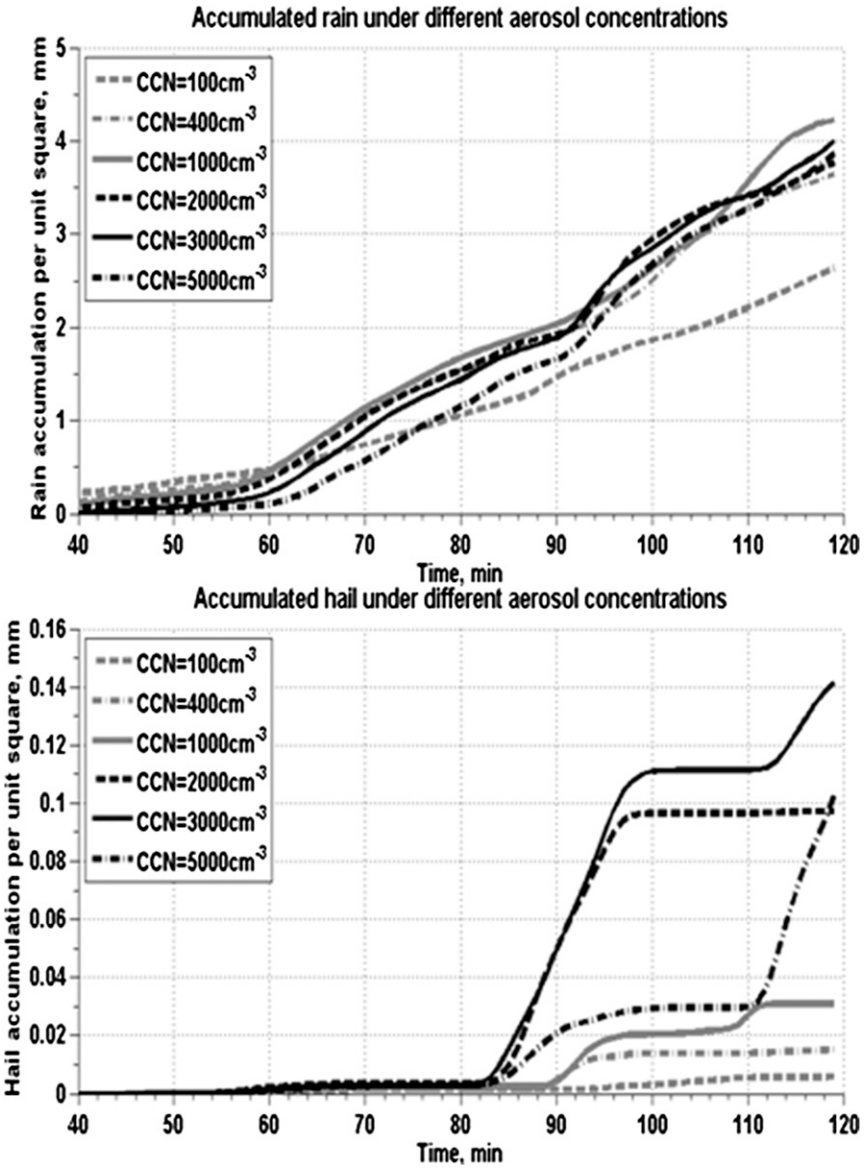

FIG. 25. Time dependencies of (top) accumulated rain at the surface and (bottom) hail precipitation (in mm of melted water) for CCN = 100, 400, 1000, 2000, 3000, and 5000 cm^{-3}.

gamma distribution (Fig. 28c) or the exponential distribution (Fig. 28d) than the local distributions.

Examples of hail number size distributions in cloud points above the freezing level are shown in Fig. 29. The size distributions are plotted in Fig. 29 for the same grid points and time instances as the mass distributions in Figs. 13 and 23. One can see that in many cases, the shape of the number size distributions with hail diameters larger than 0.5 cm resembles that of the gamma function.

In many bulk model simulations, size distributions of hail are approximated by an exponential distribution with interdependent slope, which is usually justified by the analysis of the observed hailstone size distributions at the surface. For example, Cheng et al. (1985) proposed the following empirical formula for hail-size distributions near the ground:

$$N(D) = C\Lambda^{4.11} \exp(-\Lambda D), \tag{3}$$

where Λ varies between 0.1 and 1.0 mm^{-1} and factor C varies between 60 and 300 if $N(D)$ is measured in inverse meters cubed per millimeter. The dependencies in Eq. (3) with $C = 300$ and $\Lambda = 0.4$ and 0.6 mm^{-1} are presented in Figs. 28a,b. One can see that in the H-CCN case the calculated size distribution near the surface agrees quite well with exponential distribution with $\Lambda = 0.4\,mm^{-1}$. At the

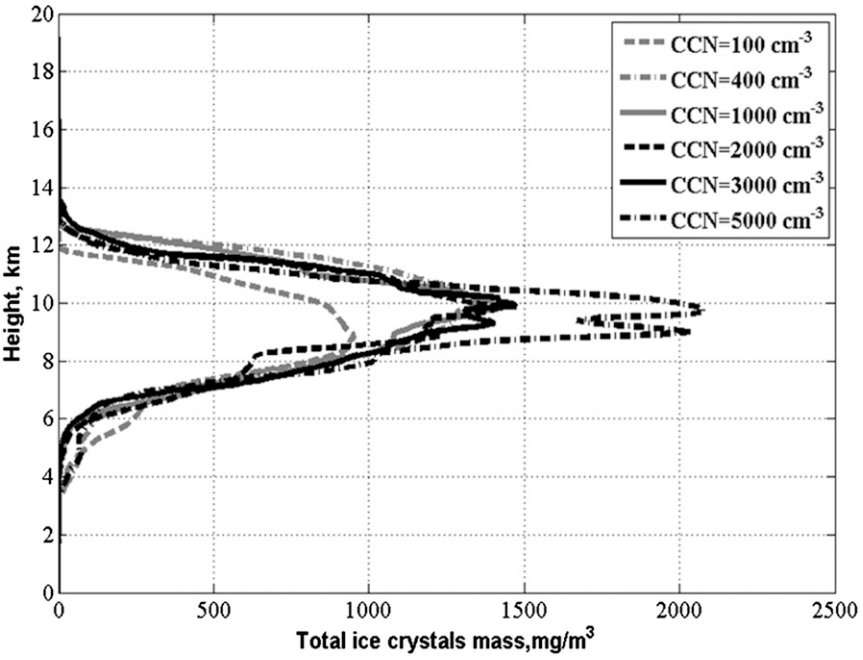

FIG. 26. Vertical profiles of maximum values of ice crystals mass content under different aerosol concentrations: CCN = 100, 400, 1000, 2000, 3000, and 5000 cm^{-3}.

same time the size distribution calculated for the L_CCN case is approximated better using $\Lambda = 0.6\,mm^{-1}$. Analysis of Figs. 28a,b and 29 shows that Λ increases with height.

The variability of the local number size distributions is very high. Figures 28c,d show that even in cases in which the shape of the number size distributions resembles that of a gamma or exponential distribution, the parameters of the distributions are quite different even at the same altitude. Moreover, the examples show that shapes of number distribution functions deviate from those of gamma distributions. For instance, calculated number distributions can be both convex and concave at different ranges of hail sizes. In many cases, slope is not constant, but changes in relation to particle size. This suggests that the hail distributions, at least in some cases, consist of several overlapping modes.

At higher altitudes, where hail distribution forms both by FD freezing and accretion of cloud droplets, the number distributions of hail are often bimodal (Fig. 29). Below freezing level, near the surface, the mode formed by smaller hail disappears because of melting, and the number size distributions become unimodal (Figs. 28a–c). The importance of the accurate description of size distribution of particles in cloud resolving models is discussed by Khain et al. (2015).

5. Summary and conclusions

In the present study, we simulated a midlatitude hail storm using a new version of HUCM spectral bin microphysics that includes a detailed description of time-dependent freezing. We studied the effects of aerosols on the production and evolution of hail and FDs, as well as on precipitation.

We found that in cases of high and low CCN concentrations, hail forms and grows via different scenarios. In the case of high CCN concentration, which is typical of continental storms, a comparatively small amount of FDs and hail forming as a result of total freezing of FDs grow by accretion of supercooled water within the area of cloud updrafts. Hail and FDs reach large sizes in the course of recycling within the comparatively narrow zone of cloud updrafts. The largest particles fall down to the surface. The hail shaft is especially strong at the decaying stage, when vertical velocity decreases such that large hail can fall through the cloud. The largest hailstones reach 5 cm in diameter. According to our results, the largest hail shaft and hail size is reached at CCN concentrations from 2000 to 3000 cm^{-3}. At these CCN concentrations, the maximum concentrations of cloud droplets in clouds are 800–1000 cm^{-3}. These droplet concentrations seem to be ''optimum'' for the formation of efficient hail growth by accretion in the course of recycling.

In contrast, at low CCN concentration, hail forms as a result of the freezing of numerous FDs forming in the vicinity of freezing level. Hail is then advected by the velocity field and spreads over a large area. The total mass of hail in clean air turns out to be larger than in

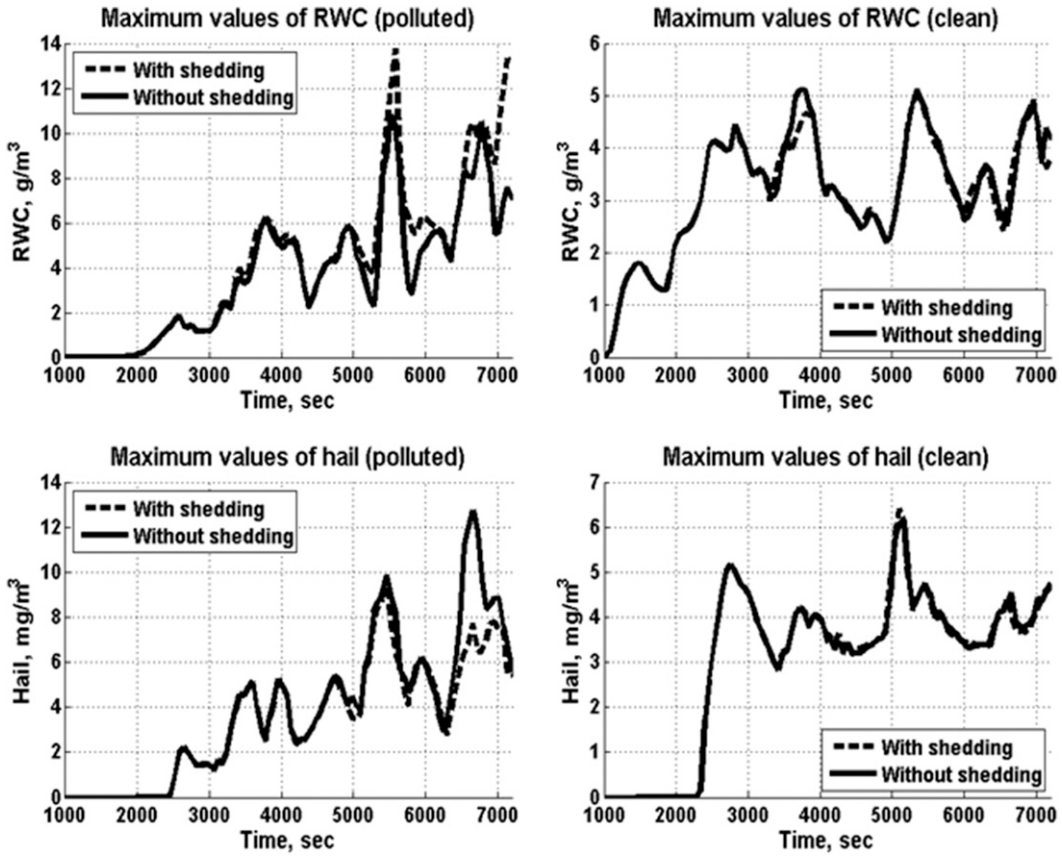

FIG. 27. Time dependencies of (top) rainwater content and (bottom) hail mass in (left) H_CCN and (right) L_CCN with shedding (dashed line) and without shedding (solid line).

H_CCN cases. At the same time, because of the lack of significant supercooled CWC, FDs and hail particles remain relatively small and largely melt, falling to the surface. As a result, the hail shaft from the H-CCN clouds turns out to be substantially stronger than the hail shaft in clean air. The process of recycling is not efficient in the case of low CCN concentration. Thus, the claim concerning the importance of the recycling process for hail growth made in a set of studies (see introduction) is valid only for cases of high CCN concentrations.

The implementation of time-dependent freezing led to an increase in HMC and hail size both at low and high CCN concentrations. While in cases of immediate freezing, the maximum hail size was around 1–2 cm (Khain et al. 2011). The implementation of time-dependent freezing allowed the simulation of hailstones with diameters of up to 5 cm. We attribute this effect first of all to the increase in the coalescence efficiency between colliding particles in cases when at least one of the colliding particles grows by wet growth. Moreover, some processes of collisions that produced graupel in the version by Khain et al. (2011) (for instance, liquid drop–snow collisions) in case of time-dependent freezing lead to FDs formation. The properties of FDs (fall velocities, sticking efficiencies) are closer to those of hail than of graupel. The production of FDs instead of graupel leads to increase of hail size especially in the L_CCN cases, when liquid drops–snow collisions are more common than in the H-CCN cases. Since FDs grow largely in the dry growth regime, full freezing takes place and FDs are converted to hail.

There are many microphysical schemes that do not describe time-dependent freezing but claim that they take into account the process of shedding. In these schemes, immediate shedding of all liquid is assumed. Taking into account time-dependent freezing allowed more accurate description of the process of shedding from hail surfaces. It allowed one to follow the history of the accretion and freezing process and to shed only part of the liquid water. This shed water was redistributed between raindrops of sizes depending on the hail Reynolds number.

Shedding decreases the size of hail particles. At the same time, shed raindrops collect supercooled cloud

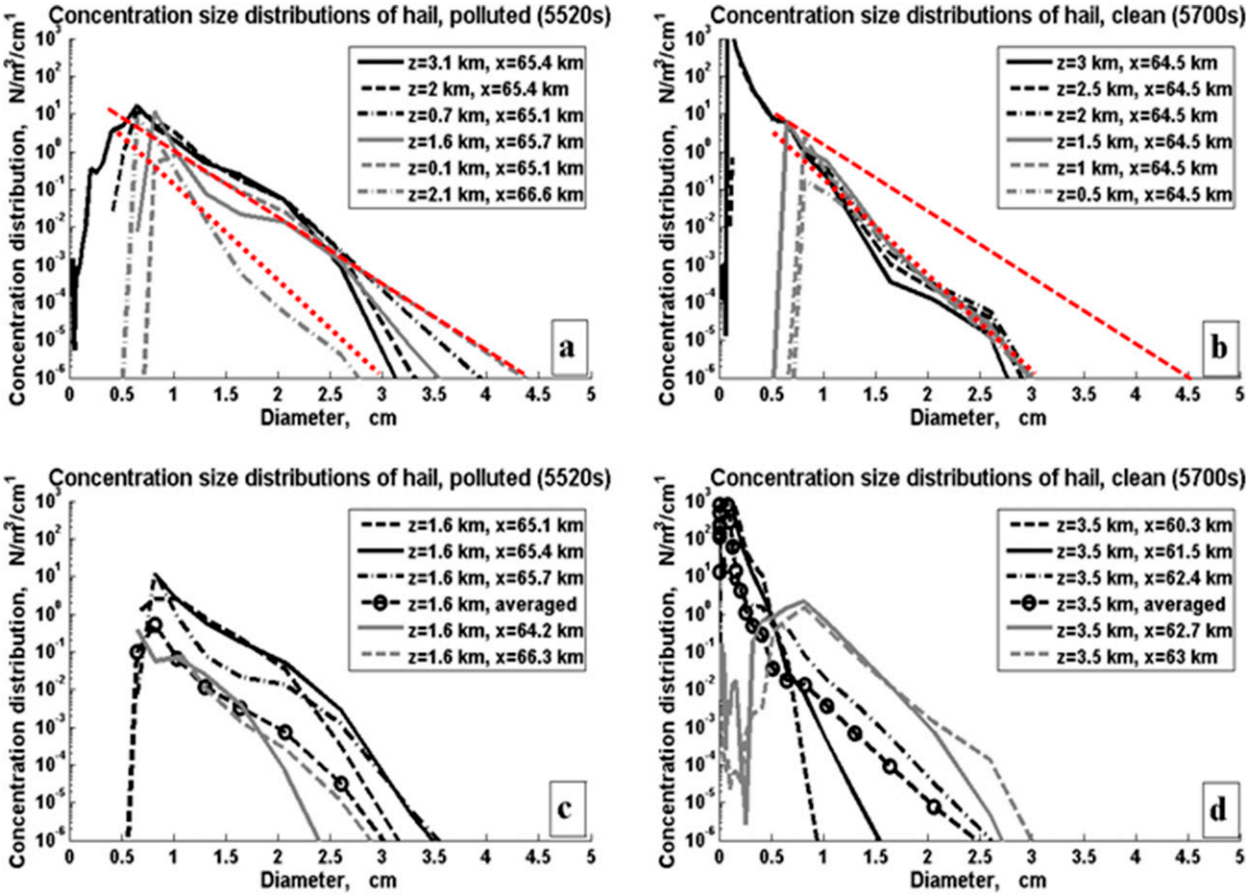

FIG. 28. Hail number concentration distribution functions below freezing level in simulations (a),(c) H_CCN and (b),(d) L_CCN at the decaying stages of convective cell evolution, when hail size reaches its maximum. The distributions at different altitudes in zones of maximum HWC: (a) $z = 3.1$, 2, and 0.7 km (black) and $z = 1.6$, 0.1, and 2.1 km (gray); (b) $z = 3$, 2.5, and 2 km (black) and $z = 1.5$, 1, and 0.5 km (gray). Empirical distributions obtained using Eq. (3) with $C = 300$ and $\Lambda = 0.4$ and 0.6 mm^{-1} are shown by red dashed and dotted lines, respectively. (c),(d) Distributions at the altitude of 1.6 and 3.5 km, respectively: $z = 1.6$ km with $x = 65.1$, 65.4, and 65.7 km (black) and $x = 64.2$ and 66.3 km (gray); $z = 3.5$ with $x = 60.3$, 61.5, and 62.4 km (black) and $x = 62.7$ and 63 km (gray); the cloud-averaged hail number distributions are shown by dashed lines with circles.

droplets and give rise to new FDs and hail. To the other effect of time-dependent freezing we can attribute the extension of the period of latent heat release and the elevation of zones of hail production. These effects are discussed in greater detail by Phillips et al. (2015).

It was also shown that FDs and hail in an H-CCN atmosphere grow by wet growth to substantially higher altitudes than in clean air. This can be attributed to the relatively large size of FDs and hail due to the high rate of accretion of supercooled drops in this case. This causes larger sizes of FDs and hail owing to a larger rate of accretion of supercooled drops.

For the first time, the processes of time-dependent dry and wet growth and the evolution of particle size distributions in the course of recycling were investigated within the frame of a multidimensional cloud model with spectral bin microphysics. It was shown that in cloud updrafts, a wet growth regime of hail takes place at higher altitudes than it does at cloud edge. As a result, during the recycling the regimes of wet and dry growth interleave. This alternation accounts for the oft-observed layered structure of hailstones (Pruppacher and Klett 1997). In principle, the model allows us to evaluate the depth of the different layers within hailstones. It was also shown that despite complicated trajectories and size sorting, there is only one size in hail-size distribution that separates the regime of dry growth for smaller hail particles from the regime of wet growth for larger hail sizes.

Finally, it was found that the accumulated masses of rain and hail that reach the surface increase with the CCN concentration up to CCN concentrations of 1000 cm^{-3}. As was shown by Khain et al. (2011), the

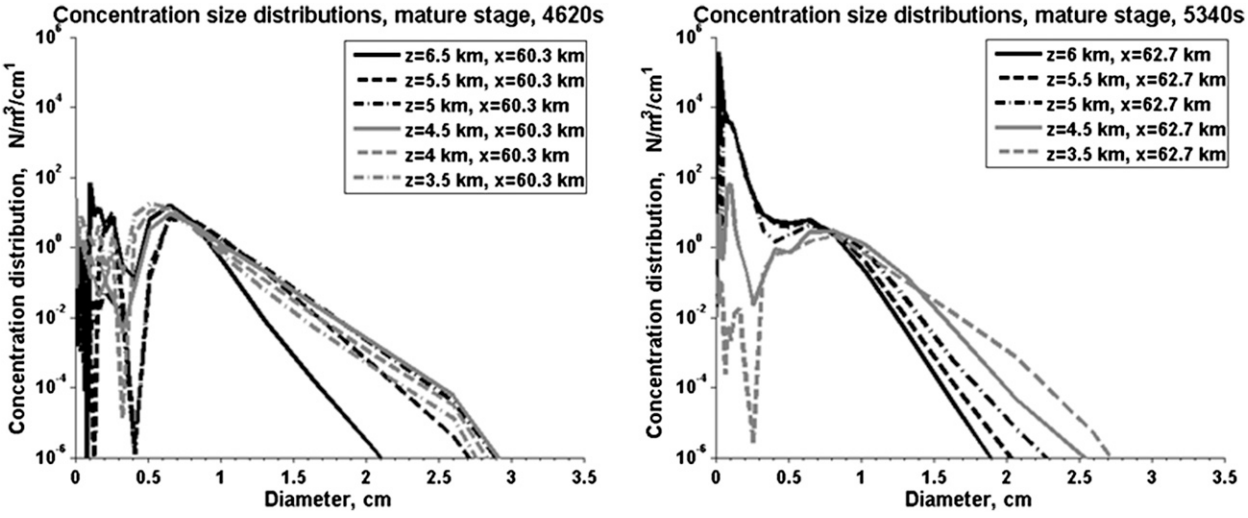

FIG. 29. Hail number concentration distribution functions below freezing level in simulations (left) H_CCN and (right) L_CCN at the mature stages of convective cell evolution. The size distributions are plotted for the same grid points and time instances as the mass size distributions in Figs. 8, 16, and 23: (left) $z = 6.5$, 5.5, and 5 km (black) and $z = 4.5$, 4, and 3.5 km (gray); (right) $z = 6$, 5.5, and 5 km (black) and $z = 4.5$, and 3.5 km (gray).

increase in accumulated rain amount is related to the high precipitation efficiency of hail. Big hail efficiently collects liquid droplets and falls to the surface without any significant loss of mass. At higher CCNs, the sensitivity of accumulated rain decreases because of an increase in hydrometeor mass loss produced through the spreading and sublimation of ice crystals in cloud anvils.

Our results are in qualitative accordance with those obtained using the previous HUCM version, the latter which did not take into account time-dependent freezing (Khain et al. 2011). In both cases, an increase in hail size with an increase in CCN concentration was reported. However, taking into account the formation of FDs on collisions led to a better representation of hail formation, especially in the clean-air cases as was discussed above. The maximum diameter of hail particles in clean-air cases was substantially less than in H_CNN cases but reached diameters of 1 cm in any case.

As was mentioned above, simulation of large hail and, especially, aerosol effects of hail size require the utilization of sophisticated microphysical schemes. A comparison of the results of the present study and of those found by Noppel et al. (2010) shows that an increase in CCN concentration leads to an increase in total hail mass in both schemes. At the same time, the results of Khain et al. (2011) and of the present study pertaining to aerosol effect on hail size and on precipitation were contra those reported by Noppel et al. (2010), where a decrease in hail size and in precipitation were reported. The discrepancy in the response of hail size to aerosols in these studies may be related to the utilization of the two-moment bulk-parameterization scheme by Noppel et al. (2010). As shown by Loftus et al. (2014) and Loftus and Cotton (2014a,b), who simulated a supercell storm that occurred over northwest Kansas on 29 June 2000 during the Severe Thunderstorm and Electrification and Precipitation Study (STEPS), it was necessary to implement three-moment bulk-parameterization scheme for hail to get the observed maximum size of hail. The analysis of two two-moment scheme used in RAMS showed that they substantially underestimated both hail mass and hail size. Simulations of a hail storm using a three-moment bulk scheme (Milbrandt and Yau 2005) seem to support the necessity of the three-moment bulk-parameterization schemes to simulate large hailstones.

The results of the three-moment bulk-parameterization scheme showed that hail size and the accumulation of hail at the surface increase with an increase in CCN concentration. So, the results of the three-moment scheme described by Loftus et al. (2014) and Loftus and Cotton (2014a,b) qualitatively agree with those of the HUCM.

Analysis of the shapes of hail number size distributions shows that in cases of intense hail shaft, the shapes of hail number distributions for largest hail particles forming in the H-CCN case are close to those obtained by Loftus et al. (2014) in their simulations of a hail storm using a bulk-parameterization scheme based on the representation of size distributions by gamma functions (not shown).

In other cases, especially above the freezing level, number distributions of hail differ substantially from the gamma distribution. Frequently, the hail spectrum turned out to be bimodal. In these cases, their approximation by gamma distributions by bulk schemes can lead to errors in reproduction of mixed-phase cloud microphysics. The mechanisms of formation of hail-size spectra require a separate investigation. Using the most recent version of HUCM, Kumjian et al. (2014) found a high correlation between the height and magnitude of differential *reflectivity* Z_{DR} columns and hail-shaft intensity. The simulations have been performed at a high CCN concentration. The next study will investigate aerosol effects on the relationships between microphysical structure and polarimetric Doppler radar signatures.

Acknowledgments. The study was supported by grants from the U.S. Department of Energy's (DoE) Office of Biological and Environmental Research (BER) (DE-S0006788; DE-SC0008811), the Binational U.S.–Israel Science Foundation (Grant 2010446), and the Israel Science Foundation (Grant 1393/14). The data can be provided upon request (alexander.khain@mail.huji.ac.il; eyal.ilotoviz@mail.huji.ac.il).

REFERENCES

Andreae, M. O., D. Rosenfeld, P. Artaxo, A. A. Costa, G. P. Frank, K. M. Longo, and M. A. F. Silva-Dias, 2004: Smoking rain clouds over the Amazon. *Science*, **303**, 1337–1342, doi:10.1126/science.1092779.

Benmoshe, N., M. Pinsky, A. Pokrovsky, and A. Khain, 2012: Turbulent effects on the microphysics and initiation of warm rain in deep convective clouds: 2-D simulations by a spectral mixed-phase microphysics cloud model. *J. Geophys. Res.*, **117**, D06220, doi:10.1029/2011JD016603.

Bigg, E. K., 1953: The formation of atmospheric ice crystals by the freezing of droplets. *Quart. J. Roy. Meteor. Soc.*, **79**, 510–519, doi:10.1002/qj.49707934207.

Bott, A., 1998: A flux method for the numerical solution of the stochastic collection equation. *J. Atmos. Sci.*, **55**, 2284–2293, doi:10.1175/1520-0469(1998)055<2284:AFMFTN>2.0.CO;2.

Browning, K. A., and G. B. Foote, 1976: Airflow and hail growth in supercell storms and some implications for hail suppression. *Quart. J. Roy. Meteor. Soc.*, **102**, 499–533, doi:10.1002/qj.49710243303.

Cheng, L., and M. English, 1983: Relationship between hailstone concentration and size. *J. Atmos. Sci.*, **40**, 204–213, doi:10.1175/1520-0469(1983)040<0204:ARBHCA>2.0.CO;2.

——, ——, and R. Wong, 1985: Hailstone size distributions and their relationship to storm thermodynamics. *J. Climate Appl. Meteor.*, **24**, 1059–1067, doi:10.1175/1520-0450(1985)024<1059:HSDATR>2.0.CO;2.

Cotton, W. C., and R. A. Anthes, 1989. *Storm and Cloud Dynamics.* Elsevier, 880 pp.

Dawson, D. T., E. R. Mansell, Y. Jung, L. J. Wicker, M. R. Kumjian, and M. Xue, 2014: Low-level ZDR signatures in supercell forward flanks: The role of size sorting and melting of hail. *J. Atmos. Sci.*, **71**, 276–299, doi:10.1175/JAS-D-13-0118.1.

——, ——, and M. R. Kumjian, 2015: Does wind shear cause hydrometeor size sorting? *J. Atmos. Sci.*, **72**, 340–348, doi:10.1175/JAS-D-14-0084.1.

Farley, R. D., and H. D. Orville, 1986: Numerical modeling of hailstorms and hailstone growth. Part I: Preliminary model verification and sensitivity tests. *J. Climate Appl. Meteor.*, **25**, 2014–2035, doi:10.1175/1520-0450(1986)025<2014:NMOHAH>2.0.CO;2.

Foote, G. B., 1984: A study of hail growth using observed storm conditions. *J. Climate Appl. Meteor.*, **23**, 84–101, doi:10.1175/1520-0450(1984)023<0084:ASOHGU>2.0.CO;2.

Freud, E., D. Rosenfeld, M. O. Andreae, A. A. Costa, and P. Artaxo, 2008: Robust relations between CCN and the vertical evolution of cloud drop size distribution in deep convective clouds. *Atmos. Chem. Phys.*, **8**, 1661–1675, doi:10.5194/acp-8-1661-2008.

Garcia-Garcia, F., and R. List, 1992: Laboratory measurements and parameterizations of supercoled water skin temperatures and bulk properties of gyrating hailstones. *J. Atmos. Sci.*, **49**, 2058–2072, doi:10.1175/1520-0469(1992)049<2058:LMAPOS>2.0.CO;2.

Hallett, J., and S. C. Mossop, 1974: Production of secondary ice particles during the riming process. *Nature*, **249**, 26–28, doi:10.1038/249026a0.

Heymsfield, A. J., 1982: A comparative study of the rates of development of potential graupel and hail embryos in High Plains storms. *J. Atmos. Sci.*, **39**, 2867–2897, doi:10.1175/1520-0469(1982)039<2867:ACSOTR>2.0.CO;2.

Khain, A. P., 2009: Notes on state-of-the-art investigations of aerosol effects on precipitation: A critical review. *Environ. Res. Lett.*, **4**, 015004, doi:10.1088/1748-9326/4/1/015004.

——, and I. L. Sednev, 1995: Simulation of hydrometeor size spectra evolution by water-water, ice-water and ice-ice interactions. *Atmos. Res.*, **36**, 107–138, doi:10.1016/0169-8095(94)00030-H.

——, and ——, 1996: Simulation of precipitation formation in the Eastern Mediterranean coastal zone using a spectral microphysics cloud ensemble model. *Atmos. Res.*, **43**, 77–110, doi:10.1016/S0169-8095(96)00005-1.

——, M. Ovtchinnikov, M. Pinsky, A. Pokrovsky, and H. Krugliak, 2000: Notes on the state-of-the-art numerical modeling of cloud microphysics. *Atmos. Res.*, **55**, 159–224, doi:10.1016/S0169-8095(00)00064-8.

——, M. Pinsky, M. Shapiro, and A. Pokrovsky, 2001: Collision rate of small graupel and water drops. *J. Atmos. Sci.*, **58**, 2571–2595, doi:10.1175/1520-0469(2001)058<2571:CROSGA>2.0.CO;2.

——, A. Pokrovsky, M. Pinsky, A. Seifert, and V. Phillips, 2004: Simulation of effects of atmospheric aerosols on deep turbulent convective clouds using a spectral microphysics mixed-phase cumulus cloud model. Part I: Model description and possible applications. *J. Atmos. Sci.*, **61**, 2963–2982, doi:10.1175/JAS-3350.1.

——, N. Benmoshe, and A. Pokrovsky, 2008: Factors determining the impact of aerosols on surface precipitation from clouds: Attempt of classification. *J. Atmos. Sci.*, **65**, 1721–1748, doi:10.1175/2007JAS2515.1.

——, D. Rosenfeld, A. Pokrovsky, U. Blahak, and A. Ryzhkov, 2011: The role of CCN in precipitation and hail in a mid-latitude storm as seen in simulations using a spectral (bin) microphysics model in a 2D dynamic frame. *Atmos. Res.*, **99**, 129–146, doi:10.1016/j.atmosres.2010.09.015.

——, V. Phillips, N. Benmoshe, and A. Pokrovsky, 2012: The role of small soluble aerosols in the microphysics of deep maritime clouds. *J. Atmos. Sci.*, **69**, 2787–2807, doi:10.1175/2011JAS3649.1.

——, T. V. Prabha, N. Benmoshe, G. Pandithurai, and M. Ovchinnikov, 2013: The mechanism of first raindrops formation in deep convective clouds. *J. Geophys. Res. Atmos.*, **118**, 9123–9140, doi:10.1002/jgrd.50641.

——, and Coauthors, 2015: Representation of microphysical processes in Cloud-Resolving Models: Spectral (bin) microphysics vs. bulk-parameterization. *Rev. Geophys.*, **53**, 247–322, doi:10.1002/2014RG000468.

Kumjian, M. R., and A. V. Ryzhkov, 2012: The impact of size sorting on the polarimetric radar variables. *J. Atmos. Sci.*, **69**, 2042–2060, doi:10.1175/JAS-D-11-0125.1.

——, A. P. Khain, N. Benmoshe, E. Ilotoviz, A. V. Ryzhkov, and V. T. J. Phillips, 2014: The anatomy and physics of ZDR columns: Investigating a polarimetric radar signature with a spectral bin microphysical model. *J. Appl. Meteor. Climatol.*, **53**, 1820–1843, doi:10.1175/JAMC-D-13-0354.1.

Levin, Z., and W. R. Cotton, 2009: *Aerosol Pollution Impact on Precipitation: A Scientific Review*. Springer, 386 pp.

Lin, Y.-L., R. D. Farley, and H. D. Orville, 1983: Bulk parameterization of the snow field in a cloud model. *J. Climate Appl. Meteor.*, **22**, 1065–1092, doi:10.1175/1520-0450(1983)022<1065:BPOTSF>2.0.CO;2.

List, R., 2014a: New hailstone physics. Part I: Heat and mass transfer (HMT) and growth. *J. Atmos. Sci.*, **71**, 1508–1520, doi:10.1175/JAS-D-12-0164.1.

——, 2014b: New hailstone physics. Part II: Results. *J. Atmos. Sci.*, **71**, 2114–2129, doi:10.1175/JAS-D-12-0165.1.

Loftus, A. M., and W. R. Cotton, 2014a: A triple-moment hail bulk microphysics scheme. Part II: Verification and comparison with two-moment bulk microphysics. *Atmos. Res.*, **150**, 97–128, doi:10.1016/j.atmosres.2014.07.016.

——, and ——, 2014b: Examination of CCN impacts on hail in a simulated supercell storm with triple-moment hail bulk microphysics. *Atmos. Res.*, **147–148**, 183–204, doi:10.1016/j.atmosres.2014.04.017.

——, ——, and G. G. Carrió, 2014: A triple-moment hail bulk microphysics scheme. Part I: Description and initial evaluation. *Atmos. Res.*, **149**, 35–57, doi:10.1016/j.atmosres.2014.05.013.

Meyers, M. P., P. J. DeMott, and W. R. Cotton, 1992: New primary ice-nucleation parameterizations in an explicit cloud model. *J. Appl. Meteor.*, **31**, 708–721, doi:10.1175/1520-0450(1992)031<0708:NPINPI>2.0.CO;2.

Milbrandt, J. A., and M. K. Yau, 2005: A multi-moment bulk microphysics parameterization. Part II: A proposed three-moment closure and scheme description. *J. Atmos. Sci.*, **62**, 3065–3081, doi:10.1175/JAS3535.1.

——, and H. Morrison, 2013: Prediction of graupel density in a bulk microphysics scheme. *J. Atmos. Sci.*, **70**, 410–429, doi:10.1175/JAS-D-12-0204.1.

Mitchell, D. L., S. K. Chai, Y. Liu, A. J. Heymsfield, and Y. Dong, 1996: Modeling cirrus clouds. Part I: Treatment of bimodal size spectra and case study analysis. *J. Atmos. Sci.*, **53**, 2952–2966, doi:10.1175/1520-0469(1996)053<2952:MCCPIT>2.0.CO;2.

Nelson, S. P., 1983: The influence of storm flow structure on hail growth. *J. Atmos. Sci.*, **40**, 1965–1983, doi:10.1175/1520-0469(1983)040<1965:TIOSFS>2.0.CO;2.

Noppel, H., A. Pokrovsky, B. Lynn, A. P. Khain, and K. D. Beheng, 2010: A spatial shift of precipitation from the sea to the land caused by introducing submicron soluble aerosols: Numerical modeling. *J. Geophys. Res.*, **115**, D18212, doi:10.1029/2009JD012645.

Phillips, V. T. J., A. Pokrovsky, and A. Khain, 2007: The influence of time-dependent melting on the dynamics and precipitation production in maritime and continental storm clouds. *J. Atmos. Sci.*, **64**, 338–359, doi:10.1175/JAS3832.1.

——, A. Khain, N. Benmoshe, A. Ryzhkov, and E. Ilotovich, 2014: Theory of time-dependent freezing. Part I: Description of scheme for wet growth of hail. *J. Atmos. Sci.*, **71**, 4527–4557, doi:10.1175/JAS-D-13-0375.1.

——, ——, ——, ——, and ——, 2015: Theory of time-dependent freezing. Part II: Scheme for freezing raindrops and simulations by a cloud model with spectral bin microphysics. *J. Atmos. Sci.*, **72**, 262–286, doi:10.1175/JAS-D-13-0376.1.

Pinsky, M., A. Khain, and M. Shapiro, 2001: Collision efficiency of drops in a wide range of Reynolds numbers: Effects of pressure on spectrum evolution. *J. Atmos. Sci.*, **58**, 742–764, doi:10.1175/1520-0469(2001)058<0742:CEODIA>2.0.CO;2.

Pruppacher, H. R., and J. D. Klett, 1997: *Microphysics of Clouds and Precipitation*. 2nd ed. Oxford Press, 963 pp.

Ramanathan, V., P. J. Crutzen, J. T. Kiehl, and D. Rosenfeld, 2001: Aerosols, climate, and the hydrological cycle. *Science*, **294**, 2119–2124, doi:10.1126/science.1064034.

Rasmussen, R. M., and A. J. Heymsfield, 1987: Melting and shedding of graupel and hail. Part I: Model physics. *J. Atmos. Sci.*, **44**, 2754–2763, doi:10.1175/1520-0469(1987)044<2754:MASOGA>2.0.CO;2.

——, V. Levizzani, and H. R. Pruppacher, 1984: A wind tunnel and theoretical study of the melting behavior of atmospheric ice particles. II: A theoretical study for frozen drops of radius < 500 μm. *J. Atmos. Sci.*, **41**, 374–380, doi:10.1175/1520-0469(1984)041<0374:AWTATS>2.0.CO;2.

Reisner, J., R. M. Rasmussen, and R. T. Bruintjes, 1998: Explicit forecasting of supercooled liquid water in winter storms using the MM5 mesoscale model. *Quart. J. Roy. Meteor. Soc.*, **124**, 1071–1107, doi:10.1002/qj.49712454804.

Rosenfeld, D., and A. Khain, 2008: Anthropogenic aerosols invigorating hail. *Proc. 15th Int. Conf. on Clouds and Precipitation*, Cancun, Mexico, ICCP, 7.5. [Available online at http://cabernet.atmosfcu.unam.mx/ICCP-2008/abstracts/Program_on_line/Oral_07/Rosenfeld_extended_2.pdf.]

——, U. Lohmann, G. B. Raga, C. D. O'Dowd, M. Kulmala, S. Fuzzi, A. Reissell, and M. O. Andreae, 2008: Flood or drought: How do aerosols affect precipitation? *Science*, **321**, 1309–1313, doi:10.1126/science.1160606.

Rotunno, R., and J. Klemp, 1985: On the rotation and propagation of simulated supercell thunderstorms. *J. Atmos. Sci.*, **42**, 271–292, doi:10.1175/1520-0469(1985)042<0271:OTRAPO>2.0.CO;2.

Seifert, A., and K. D. Beheng, 2006: A two-moment cloud microphysics parameterization for mixed-phase clouds. Part 1: Model description. *Meteor. Atmos. Phys.*, **92**, 45–66, doi:10.1007/s00703-005-0112-4.

Seigel, R. B., and S. C. van den Heever, 2013: Squall-line intensification via hydrometeor recirculation. *J. Atmos. Sci.*, **70**, 2012–2031, doi:10.1175/JAS-D-12-0266.1.

Takahashi, T., 1976: Hail in an axisymmetric cloud model. *J. Atmos. Sci.*, **33**, 1579–1601, doi:10.1175/1520-0469(1976)033<1579:HIAACM>2.0.CO;2.

——, T. Endoh, and G. Wakahama, 1991: Vapor diffusional growth of free-falling snow crystals between −3 and −23°C. *J. Meteor. Soc. Japan*, **69**, 15–30.

Tao, W.-K., X. Li, A. Khain, T. Matsui, S. Lang, and J. Simpson, 2007: Role of atmospheric aerosol concentration on deep convective precipitation: Cloud-resolving model simulations. *J. Geophys. Res.*, **112**, D24S18, doi:10.1029/2007JD008728.

——, J.-P. Chen, Z. Li, C. Wang, and C. Zhang, 2012: Impact of aerosols on convective clouds and precipitation. *Rev. Geophys.*, **50**, RG2001, 10.1029/2011RG000369.

Tessendorf, S. A., L. J. Miller, K. C. Wiens, and S. A. Rutledge, 2005: The 29 June 2000 supercell observed during STEPS. Part I: Kinematics and microphysics. *J. Atmos. Sci.*, **62**, 4127–4150, doi:10.1175/JAS3585.1.

Vali, G., 1994: Freezing rate due to heterogeneous nucleation. *J. Atmos. Sci.*, **51**, 1843–1856, doi:10.1175/1520-0469(1994)051<1843:FRDTHN>2.0.CO;2.

Wisner, C., H. D. Orville, and C. Myers, 1972: A numerical model of a hail-bearing cloud. *J. Atmos. Sci.*, **29**, 1160–1181, doi:10.1175/1520-0469(1972)029<1160:ANMOAH>2.0.CO;2.